Geochemistry, Geophysics, Geosystems®

RESEARCH ARTICLE
10.1029/2025GC012263

A Coral Biomineralization Model for Dual Clumped Isotopes

James M. Watkins[1], Qicui Jia[2], Shuo Zhang[2], Laurent S. Devriendt[3], and Sang Chen[4]

[1]Department of Earth and Planetary Sciences, University of California, Davis, CA, USA, [2]Department of Hydraulic Engineering, Beijing, China, [3]Chemical Sciences Division, Lawrence Berkeley National Laboratory, Berkeley, CA, USA, [4]School of Oceanography, Shanghai Jiao Tong University, Shanghai, China

Abstract Corals exhibit larger and more variable deviations from equilibrium in stable isotope composition ($\delta^{13}C$, $\delta^{18}O$, Δ_{47} and Δ_{48}) than most marine biocalcifiers. The disequilibrium isotope effects complicate paleoclimate applications but offer a window into biocalcification processes. Here, we merge a Δ_{47}-Δ_{48} isotope model in the $CaCO_3$-DIC-H_2O system (Watkins & Devriendt, 2022, https://doi.org/10.1029/2021gc010200) with a coral biomineralization model (Chen et al., 2018, https://doi.org/10.1016/j.gca.2018.02.032) and compare its outputs to recent isotopic measurements. The model simultaneously fits the data from multiple coral species but requires a different set of parameters for deep-sea corals versus tropical corals. We find that: (a) Deviations from dual clumped isotope equilibrium are due primarily to the CO_2 hydration reaction, the reversibility of which is modulated by the enzyme carbonic anhydrase (CA), the strength of the biological proton pump, and the kinetics of calcification. (b) Optimal data-model agreement for both $\delta^{13}C$-$\delta^{18}O$ and Δ_{47}-Δ_{48} is achieved where CA increases the CO_2 hydration reaction rate by ~2,000x for deep-sea corals and by 1–500x for tropical corals. (c) The Δ_{47}-Δ_{48} co-variation slope is sensitive to the cellular CO_2 flux relative to the seawater DIC flux, with higher cellular CO_2 and/or lower seawater throughput favoring a shallower slope. (d) For the most part, the modeled compositions of the calcifying fluids (e.g., pH, $[CO_3^{2-}]$, $[Ca^{2+}]$) are in good agreement with *in-situ* measurements. The data-model agreement constitutes an important step toward a general quantitative biocalcification model applicable to a wide variety of calcifying organisms.

Plain Language Summary The stable isotope composition of minerals can be used to infer the conditions of mineral growth. This approach works well for most marine biominerals, but corals present a unique challenge: their skeletons record environmental conditions but the signals are also influenced by biological processes. We use stable isotope data from recent work and develop a process-based model of coral growth to investigate the sensitivity of coral isotope compositions to biological processes (e.g., alkalinity pumping) as well as changes in the external environment such as seawater pH and temperature.

Key Points:

- We develop a process-based biomineralization model for dual-clumped isotopes
- The model explains $\delta^{13}C$-$\delta^{18}O$ and Δ_{47}-Δ_{48} co-variations among coral samples
- Dual clumped isotopes constrain the composition of the calcifying fluid in corals

Supporting Information:

Supporting Information may be found in the online version of this article.

Correspondence to:

J. M. Watkins,
jamwatkins@ucdavis.edu

Citation:

Watkins, J. M., Jia, Q., Zhang, S., Devriendt, L. S., & Chen, S. (2025). A coral biomineralization model for dual clumped isotopes. *Geochemistry, Geophysics, Geosystems*, *26*, e2025GC012263. https://doi.org/10.1029/2025GC012263

Received 28 FEB 2025
Accepted 24 JUN 2025

Author Contributions:

Conceptualization: James M. Watkins, Qicui Jia, Shuo Zhang, Laurent S. Devriendt, Sang Chen
Investigation: James M. Watkins, Qicui Jia, Shuo Zhang, Laurent S. Devriendt, Sang Chen
Methodology: James M. Watkins, Qicui Jia, Shuo Zhang, Sang Chen
Project administration: James M. Watkins
Resources: James M. Watkins, Shuo Zhang
Software: James M. Watkins, Qicui Jia
Validation: James M. Watkins, Qicui Jia

1. Introduction

Biogenic carbonate minerals (e.g., corals, foraminifera, mollusks, brachiopods, otoliths, coccoliths) record environmental conditions via their trace element and stable isotope compositions. Corals are a particularly attractive target for paleoclimate reconstructions because a coral colony develops at a fixed location and its aragonite skeleton grows daily (Wells, 1963), offering an archive of seawater conditions with extraordinary temporal resolution. Seasonally resolved tropical coral $\delta^{18}O$ records spanning multiple decades to centuries have been obtained since the early work of Fairbanks and Dodge (1979) and led to reconstructions of past climate variability in the Pacific and Indian Oceans (e.g., Abram et al., 2007, 2008; Cobb et al., 2003; Cobb et al., 2013; Cole et al., 1993; Corrège et al., 2004; Dunbar et al., 1994; Freund et al., 2019; McGregor & Gagan, 2004; Tierney et al., 2015; Tudhope et al., 2001).

The use of corals in paleoclimate research is not without complications. The carbon and oxygen compositions of coral aragonite ($\delta^{13}C$, $\delta^{18}O$) have long been recognized as anomalous in comparison to other marine biocalcifiers (Adkins et al., 2003; McConnaughey, 1989a; Weber & Woodhead, 1972). Asymbiotic coral species growing near the surface and in the deep sea display strongly correlated negative departures from equilibrium in $\delta^{13}C$ and $\delta^{18}O$ within individual specimens (Adkins et al., 2003; Emiliani et al., 1978; McConnaughey, 1989a; Weber & Woodhead, 1970). Similarly, symbiotic corals display negative $\delta^{13}C$ and $\delta^{18}O$ deviations from equilibrium but with significantly smaller within-specimen variation and a weaker $\delta^{13}C$-$\delta^{18}O$ covariation (McConnaughey, 1989a; Weber & Woodhead, 1972). The Δ_{47} compositions of asymbiotic and symbiotic corals are also anomalous, exhibiting positive departures from equilibrium (Saenger et al., 2012; Spooner et al., 2016). This is in

Writing – original draft: James M. Watkins, Shuo Zhang, Laurent S. Devriendt
Writing – review & editing: James M. Watkins, Qicui Jia, Shuo Zhang, Laurent S. Devriendt, Sang Chen

contrast to Δ_{47} data from foraminifera (Grauel et al., 2013; Henkes et al., 2013; Meinicke et al., 2020; Peral et al., 2018; Piasecki et al., 2019; Tripati et al., 2010), mollusks (Eagle et al., 2013; Henkes et al., 2013), brachiopods, (Came et al., 2014), and coccolithophorids (Katz et al., 2017; Tripati et al., 2010), all of which share a common Δ_{47}-T relationship with inorganic calcite that is within error of the expectation for clumped isotope equilibrium.

Dual clumped isotope measurements (Δ_{47} and Δ_{48}) have emerged as a new tool for identifying the causes of clumped isotope disequilibrium in coral aragonite (Guo, 2020) and to correct Δ_{47} for kinetic biases that obscure the temperature of mineral formation (Bajnai et al., 2020; Davies et al., 2022, 2023; Fiebig et al., 2021). To enable accurate interpretation of Δ_{47}-Δ_{48} data, a theoretical framework is needed. Previous efforts to model kinetic stable isotope effects in corals have focused on reaction kinetics in the DIC-H_2O system without taking into account the role of $CaCO_3$ precipitation (Davies et al., 2022; Guo, 2020; Rollion-Bard et al., 2011; Saenger & Erez, 2016). These models also do not account for important aspects of coral physiology such as proton pumping (variable pH regulation), symbiont activity, and cross-membrane CO_2 transport, all of which are expected to influence stable isotope fractionation in corals (Adkins et al., 2003; Chen et al., 2018; McConnaughey, 1989a, 1989b).

In this contribution, we take a coral biocalcification model that was developed to explain $\delta^{13}C$-$\delta^{18}O$ observations (Chen et al., 2018), update it with recently revised kinetic and equilibrium fractionation factors (Christensen et al., 2021; Guo, 2020; Yumol et al., 2020; Zeebe, 2020), and extend it to dual-clumped isotopes using the COAD box model infrastructure of Watkins and Devriendt (2022). Following an optimization step for seawater residence time and cell membrane permeability, the model reproduces the trends in all four isotopic measurements. The modeled composition of the calcifying fluid (CF) is compared to independent estimates, and the data-model comparison enables us to further constrain the biological parameters responsible for deviations from isotopic equilibrium in corals. This modeling framework will be useful to paleoceanographic reconstructions as dual clumped isotope measurements become more widespread.

2. Data Description

2.1. Notation

Carbon and oxygen isotope compositions are reported in standard delta notation:

$$\delta^{13}C(‰) = 1000 \times \left(\frac{\left({}^{13}C/{}^{12}C\right)_{sample}}{\left({}^{13}C/{}^{12}C\right)_{standard}} - 1 \right) \quad (1)$$

and

$$\delta^{18}O(‰) = 1000 \times \left(\frac{\left({}^{18}O/{}^{16}O\right)_{sample}}{\left({}^{18}O/{}^{16}O\right)_{standard}} - 1 \right). \quad (2)$$

While the $\delta^{13}C$ and $\delta^{18}O$ of the carbonate phases are reported on the VPDB scale, the $\delta^{18}O$ of water is on the VSMOW scale. The equation for converting the $\delta^{18}O$ of water from the VSMOW to VPDB scales is (Hillaire-Marcel et al., 2021):

$$\delta^{18}O_{VPDB}(‰) = 0.97001 \times \delta^{18}O_{VSMOW}(‰) - 29.99. \quad (3)$$

We hereafter drop the VPDB subscript and note that all carbon and oxygen isotope delta values are expressed on the VPDB scale unless otherwise noted.

Clumped isotope compositions are reported in standard Delta notation:

$$\Delta_{47}(‰) = \left(\frac{R_{47}}{R^*_{47}} - 1 \right) \quad (4)$$

and

Table 1
Seawater Conditions for the Different Groups of Coral Samples

Group	Sample ID	Genus	Species	Depth (m)	T (°C)	$\delta^{18}O_{sw}$ VSMOW (‰)	$\delta^{13}C_{DIC}$ VPDB (‰)
Cold water	LP01	*Desmophyllum*	*pertusum*	573	13.5	1.16	0.76
	LP02	*Desmophyllum*	*pertusum*	881	9.0	0.4	0.72
	LP03	*Desmophyllum*	*pertusum*	558	7.9	0.17	0.59
	LP04	*Desmophyllum*	*pertusum*	250	5.9	0.18	0.49
	MO01	*Madrepora*	*oculata*	573	13.5	1.16	0.76
	SV01	*Solenosmilia*	*variabilis*	1,100	5.0	–	–
	JR01	*Desmophyllum*	*pertusum*	323	7.2	0.29	0.79
	DD01	*Desmophyllum*	*dianthus*	573	13.5	1.16	0.76
	LP-SM-U	*Desmophyllum*	*pertusum*	374	9.2	–	–
Average					**9.4**	**0.65**	**0.69**
Warm water	PG1	*Porites*	*lutea*	1	29.3	0.52	1.6
	A4	*Acropora*	*cervicornis*	6	28.5	1.2	1.8
	DS3	*Pseudodiploria*	*strigosa*	6	28.5	1.2	1.8
	A6	*Acropora*	*sp.*	1	29.3	0.52	1.6
	PL7	*Porites*	*lutea*	1	26	1.7	–
	Q43	*Porites*	*lutea*	1	26	1.7	–
	SA5	*Siderastrea*	*siderea*	1	28.5	1.2	1.8
Average					**28.0**	**1.15**	**1.72**

Note. Values in bold are those used in simulations.

$$\Delta_{48}(‰) = \left(\frac{R_{48}}{R^*_{48}} - 1\right), \quad (5)$$

where R_i represents the i/44 isotopologue ratio and R^*_i the stochastic i/44 isotopologue ratio.

2.2. Samples

The two data sets used herein include measurements of $\delta^{13}C$-$\delta^{18}O$ (Adkins et al., 2003) and $\delta^{13}C$-$\delta^{18}O$-Δ_{47}-Δ_{48} (Davies et al., 2022). The $\delta^{13}C$-$\delta^{18}O$ data in Adkins et al. (2003) were collected by micro sampling the thecal region (47407-G) and septal region (47407-2A) of the deep-sea coral *Desmophyllum dianthus*. The sample was collected at a depth of 549 m, with a seawater temperature of 5.5 ± 1°C, $\delta^{18}O_{sw}$ of 0.3 ± 0.2 and $\delta^{13}C_{DIC}$ of 0.6 ± 0.4. Each measurement involved the collection of approximately 40 μg of aragonite powder, and the isotopic results showed variation of $\delta^{13}C$-$\delta^{18}O$ perpendicular to the coral's banding.

Davies et al. (2022) analyzed coral samples from both deep-sea and tropical environments (Table 1). The tropical coral samples are from four locations and include five species: *Porites lutea, Acropora cervicornis, Acropora sp., Pseudodiploria strigose* and *Siderastrea siderea*. The samples were collected at depths ranging from 1 to 6 m, with a seawater temperature of 28.0 ± 2.0°C, $\delta^{18}O_{sw}$ of 1.15 ± 0.48 and $\delta^{13}C_{DIC}$ of 1.72 ± 0.11. The samples were cut from inner cores of corals and were about 0.5 cm thick. The deep-sea corals were collected from seven sampling sites and the specimens include *Desmophyllum pertusum, Madrepora oculata, Solenosmilia variabilis* and *D. dianthus*. These samples were collected from depths ranging from 250 to 1,100 m, with a seawater temperature of 9.4 ± 4.5°C, $\delta^{18}O_{sw}$ of 0.65 ± 0.48 and $\delta^{13}C_{DIC}$ of 0.69 ± 0.11. Notably, only the theca walls were sampled for the deep-sea coral. Davies et al. (2022) analyzed $\delta^{13}C$-$\delta^{18}O$-Δ_{47}-Δ_{48} simultaneously, requiring approximately 10 mg of aragonite powder per sample.

In summary, the isotopic data from Adkins et al. (2003) reflect the variable isotopic composition of the same coral species perpendicular to its banding pattern, while the data from Davies et al. (2022) include samples from

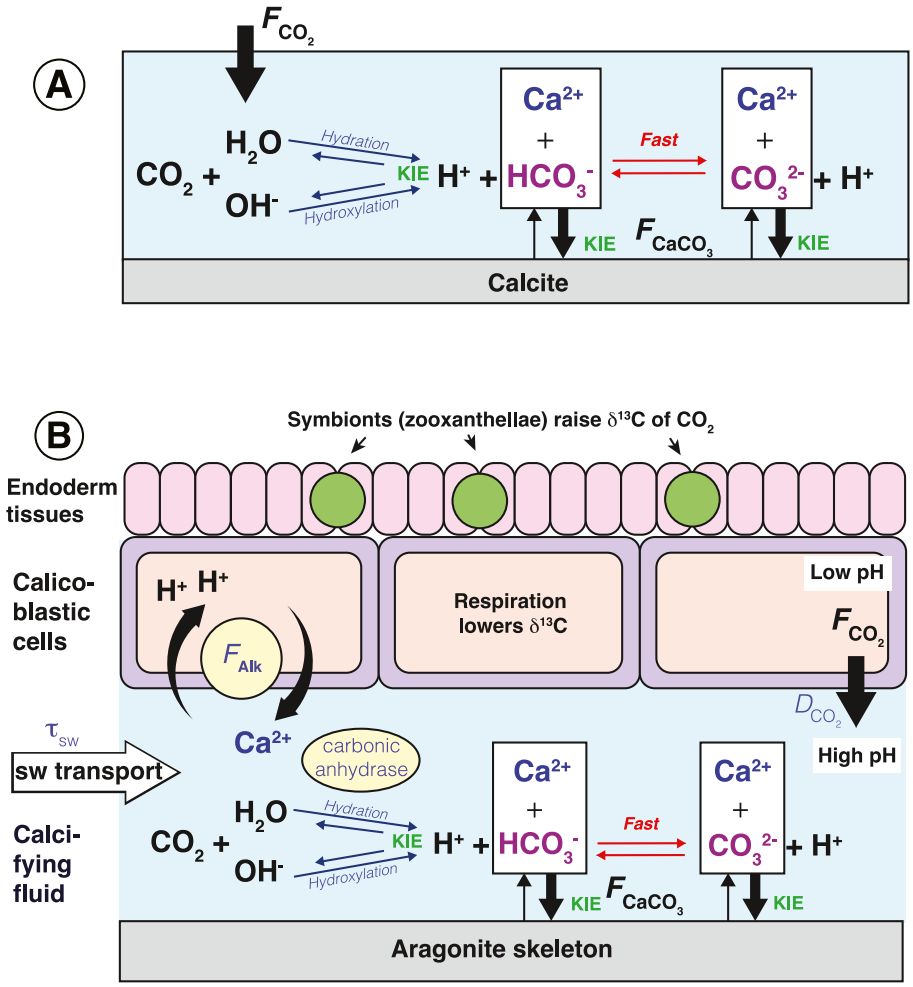

Figure 1. (a) Schematic showing the physicochemical rules of inorganic calcite precipitation from a CO_2-fed solution and the reactions that contribute to kinetic isotope effects, as in Watkins and Devriendt (2022). (b) Schematic of the coral biocalcification model of Chen et al. (2018) showing the molecular fluxes in and out of the calcification space. The two carbon sources are seawater DIC and cellular CO_2. The carbon isotopic composition of cellular CO_2 can be altered by symbiont activity in the endoderm tissues and by respiration in tissue cells. Once in the calcifying fluid, the cellular CO_2 undergoes hydration and hydroxylation to produce isotopically light HCO_3^- and CO_3^{2-}. By contrast, the seawater flux brings in isotopically equilibrated HCO_3^- and CO_3^{2-}. Modified from Chen and Watkins (2025).

multiple locations and species. However, the $\delta^{13}C$-$\delta^{18}O$ trends within coral (Adkins et al., 2003) and between coral (Davies et al., 2022) are similar, suggesting similar control mechanisms.

3. Coral Biomineralization Model

3.1. Physicochemical Rules of Precipitation

A box model for the dual-clumped isotope composition of $CaCO_3$ precipitating from a CO_2-fed solution was developed by Watkins and Devriendt (2022) (Figure 1a). The brief overview here summarizes the model framework and defines the kinetic fractionation factors (KFFs) referenced throughout the discussion.

The Watkins and Devriendt (2022) model includes a user-specified CO_2 influx, complete DIC-H_2O reaction kinetics, and a $CaCO_3$ outflux that is calculated based on growth laws for inorganic $CaCO_3$. The two key reactions for kinetic isotope effects (KIEs) are the relatively slow hydration and hydroxylation reactions:

$$CO_2 + H_2O \underset{k_{-1}}{\overset{k_{+1}}{\rightleftharpoons}} HCO_3^- + H^+ \quad (6)$$

and

$$CO_2 + OH^- \underset{k_{-4}}{\overset{k_{+4}}{\rightleftharpoons}} HCO_3^-, \quad (7)$$

where the k's are rate constants. For the isotopologue-specific versions of these reactions, we use the following shorthand notation: $^{12}C = 2$, $^{13}C = 3$, $^{16}O = 6$, and $^{18}O = 8$. We also drop the superscript charges on ionic species (e.g., [H^+ becomes H, etc.) such that these reactions become:

$$266 + H_26 \underset{k_{-1}}{\overset{k_{+1}}{\rightleftharpoons}} H2666 + H \quad (8)$$

and

$$266 + 6H \underset{k_{-4}}{\overset{k_{+4}}{\rightleftharpoons}} H2666. \quad (9)$$

For carbon isotopes we have:

$$366 + H_26 \underset{c_{-1}}{\overset{c_{+1}}{\rightleftharpoons}} H3666 + H \quad (10)$$

and

$$366 + 6H \underset{c_{-4}}{\overset{c_{+4}}{\rightleftharpoons}} H3666. \quad (11)$$

For oxygen isotopes, we have:

$$266 + H_28 \underset{1/3a_{-1}}{\overset{a_{+1}}{\rightleftharpoons}} H2866 + H, \quad (12)$$

$$286 + H_26 \underset{2/3b_{-1}}{\overset{b_{+1}}{\rightleftharpoons}} H2866 + H, \quad (13)$$

$$266 + 8H \underset{1/3a_{-4}}{\overset{a_{+4}}{\rightleftharpoons}} H2866, \quad (14)$$

and

$$286 + 6H \underset{2/3b_{-4}}{\overset{b_{+4}}{\rightleftharpoons}} H2866. \quad (15)$$

For ^{13}C-^{18}O clumped isotopes, we have:

$$366 + H_28 \underset{1/3p_{-1}}{\overset{p_{+1}}{\rightleftharpoons}} H3866 + H, \quad (16)$$

$$386 + H_26 \underset{2/3s_{-1}}{\overset{s_{+1}}{\rightleftharpoons}} H3866 + H, \quad (17)$$

$$366 + 8H \underset{1/3p_{-4}}{\overset{p_{+4}}{\rightleftharpoons}} H3866, \tag{18}$$

and

$$386 + 6H \underset{2/3s_{-4}}{\overset{s_{+4}}{\rightleftharpoons}} H3866. \tag{19}$$

For ^{18}O-^{18}O clumped isotopes, we have:

$$286 + H_2 8 \underset{2/3p'_{-1}}{\overset{p'_{+1}}{\rightleftharpoons}} H2886 + H, \tag{20}$$

$$288 + H_2 6 \underset{1/3s'_{-1}}{\overset{s'_{+1}}{\rightleftharpoons}} H2886 + H, \tag{21}$$

$$286 + 8H \underset{2/3p'_{-4}}{\overset{p'_{+4}}{\rightleftharpoons}} H2886, \tag{22}$$

and

$$288 + 6H \underset{1/3s'_{-4}}{\overset{s'_{+4}}{\rightleftharpoons}} H2886. \tag{23}$$

The rate constants follow the notation of Uchikawa et al. (2021) and the 1/3 and 2/3 factors are necessary for oxygen isotope book-keeping (cf. Watkins & Devriendt, 2022). The isotopologue rate constants normalized by the k's define the KFFs; for example, the hydration KFF for carbon isotopes is $c_{+1}/k_{+1} = 0.982$, which means that carbon isotopes are fractionated by 18‰ during unidirectional hydration (assuming no isotopic distillation of reactant CO_2).

The other set of reactions that contribute to KIEs are the crystal growth reactions:

$$Ca^{2+} + HCO_3^- \underset{\nu_{B_2}}{\overset{k_{B_2}}{\rightleftharpoons}} CaCO_3 + H^+ \tag{24}$$

and

$$Ca^{2+} + CO_3^{2-} \underset{\nu_{B_1}}{\overset{k_{B_1}}{\rightleftharpoons}} CaCO_3, \tag{25}$$

where the k's and ν's are rate constants following the notation of Wolthers et al. (2012). Importantly, all of the forward rate constants for the hydration, hydroxylation, and crystal growth reactions are "known" (Table 2; Section S1 in Supporting Information S1). The backward reaction rate constants can be calculated from the forward rate constants and equilibrium constraints. These reactions in the $CaCO_3$-DIC-H_2O system constitute the physicochemical rules of carbonate precipitation in the absence of biological or "vital" effects. We built upon this framework by adding fluxes that are relevant for biogenic $CaCO_3$ precipitation.

3.2. Biological Components

Decades of research from biophysical, morphological and geochemical perspectives have led to an integrated model for coral biomineralization (Figure 1b). The CF is envisaged as being a thin (~10 μm) region at the interface between living tissue and skeleton (Cohen & McConnaughey, 2003). Previously identified biomineralization processes relevant to aragonite growth kinetics and isotopic partitioning include: (a) Transfer of seawater to the calcifying space through passive leakage or active vacuolization, or transmembrane transport of

Table 2
Isotopic Rate Constants for the Hydration and Hydroxylation Reactions

Description	KFF	Chen value	Our value	Reference
H_2O fractionation–hydration	a_{+1}/k_{+1}	0.993	0.991	Yumol et al. (2020)
CO_2 fractionation–hydration	b_{+1}/k_{+1}	0.990	0.997	Yumol et al. (2020)
OH^- fractionation–hydroxylation	a_{+4}/k_{+4}	0.993	0.971	Watkins and Devriendt (2022)
CO_2 fractionation–hydroxylation	b_{+4}/k_{+4}	0.990	1.000	Clark et al. (1992)
$^{13}C/^{12}C$ fractionation–hydration	c_{+1}/k_{+1}	0.987	0.982	Yumol et al. (2020)
$^{13}C/^{12}C$ fractionation–hydroxylation	c_{+4}/k_{+4}	0.989	0.981	Christensen et al. (2021)
^{13}C-^{18}O–hydration	p_{+1}/k_{+1}	–	$\approx \frac{c_{+1}}{k_{+1}} \cdot \frac{a_{+1}}{k_{+1}}$	Uchikawa et al. (2021)
^{13}C-^{18}O–hydration	s_{+1}/k_{+1}	–	$\approx \frac{c_{+1}}{k_{+1}} \cdot \frac{b_{+1}}{k_{+1}}$	Uchikawa et al. (2021)
^{13}C-^{18}O–hydroxylation	p_{+4}/k_{+4}	–	$\approx \frac{c_{+4}}{k_{+4}} \cdot \frac{a_{+4}}{k_{+4}}$	Uchikawa et al. (2021)
^{13}C-^{18}O–hydroxylation	s_{+4}/k_{+4}	–	$\approx \frac{c_{+4}}{k_{+4}} \cdot \frac{b_{+4}}{k_{+4}}$	Uchikawa et al. (2021)
^{18}O-^{18}O–hydration	p'_{+1}/k_{+1}	–	$\approx \frac{b_{+1}}{k_{+1}} \cdot \frac{a_{+1}}{k_{+1}}$	Uchikawa et al. (2021)
^{18}O-^{18}O–hydration	s'_{+1}/k_{+1}	–	$\approx \frac{b_{+1}}{k_{+1}} \cdot \frac{b_{+1}}{k_{+1}}$	Uchikawa et al. (2021)
^{18}O-^{18}O–hydroxylation	p'_{+4}/k_{+4}	–	$\approx \frac{b_{+4}}{k_{+4}} \cdot \frac{a_{+4}}{k_{+4}}$	Uchikawa et al. (2021)
^{18}O-^{18}O–hydroxylation	p'_{+4}/k_{+4}	–	$\approx \frac{b_{+4}}{k_{+4}} \cdot \frac{b_{+4}}{k_{+4}}$	Uchikawa et al. (2021)
$CaCO_3$-CO_3	$^{18}k_{B_1}/k_{B_1}$	–	0.9995	Watkins and Devriendt (2022)
$CaCO_3$-HCO_3	$^{18}k_{B_2}/k_{B_2}$	–	0.9966	Watkins and Devriendt (2022)
$CaCO_3$-CO_3	$^{13}k_{B_1}/k_{B_1}$	–	1.0005	Romanek et al. (1992)
$CaCO_3$-HCO_3	$^{13}k_{B_2}/k_{B_2}$	–	1.0005	Romanek et al. (1992)
$CaCO_3$-CO_3	$^{13-18}k_{B_1}/k_{B_1}$	–	$\approx \frac{^{18}k_{B_1}}{k_{B_1}} \cdot \frac{^{13}k_{B_1}}{k_{B_1}}$	Watkins and Devriendt (2022)
$CaCO_3$-HCO_3	$^{13-18}k_{B_2}/k_{B_2}$	–	$\approx \frac{^{18}k_{B_2}}{k_{B_2}} \cdot \frac{^{13}k_{B_2}}{k_{B_2}}$	Watkins and Devriendt (2022)
$CaCO_3$-CO_3	$^{18-18}k_{B_1}/k_{B_1}$	–	$\approx \frac{^{18}k_{B_1}}{k_{B_1}} \cdot \frac{^{18}k_{B_1}}{k_{B_1}}$	Watkins and Devriendt (2022)
$CaCO_3$-HCO_3	$^{18-18}k_{B_2}/k_{B_2}$	–	$\approx \frac{^{18}k_{B_2}}{k_{B_2}} \cdot \frac{^{18}k_{B_2}}{k_{B_2}}$	Watkins and Devriendt (2022)

Note. The carbon and oxygen KFFs have been updated since Chen et al. (2018). For dual clumped isotopes, the KFFs are expressed as functions of the carbon and oxygen isotope KFFs.

ions (through pumps or channels) to the site of calcification (Ip & Krishnaveni, 1991; Kinsman, 1969), (b) a flux of CO_2 from the high [CO_2] tissue adjacent to the CF (Al-Horani et al., 2003b), (c) active H^+ removal from the CF coupled with cation pumping to the calcifying space facilitated by ion transporters such as Ca-ATPase (Al-Horani et al., 2003a; Kingsley & Watabe, 1984; Yu & Inesi, 1995), (d) The presence of the enzyme carbonic anhydrase (CA), which catalyzes the conversion of CO_2 to HCO_3^- in the CF (Kingsley & Watabe, 1987; Mass et al., 2014; Moya et al., 2008; Tambutté et al., 2007), and (e) aragonite precipitation. The above processes can be expressed mathematically in the following ways (cf. Chen et al., 2018):

1. The process(es) by which seawater gets transported to the calcifying space are lumped together and the seawater contribution is quantified using a generalized seawater turnover timescale (τ_{sw} in s).
2. The flux of (CO_2) from the cellular space is quantified using a membrane permeability coefficient (D_{cell} in m/s) that is on the order of 10^{-5} m/s (Sültemeyer & Rinast, 1996). This cellular CO_2 flux is assumed to have the same $\delta^{18}O$, Δ_{47}, and Δ_{48} as seawater CO_2 but may have a different $\delta^{13}C$ due to respiration (lower $\delta^{13}C$) or photosynthesis in symbiotic corals (higher $\delta^{13}C$; Swart, 1983). Changes in the $\delta^{13}C$ of the DIC reservoir caused by photosynthesis and respiration are termed "metabolic" isotope effects (McConnaughey, 1989a).
3. A cation alkalinity pump (F_{Alk}) increases the pH of the CF by exchanging two H^+ for one Ca^{2+}. If other cations are involved in exchanging for H^+, then the Ca^{2+} fraction of the alkalinity pump (f_{Ca}) can be decreased accordingly.

4. The influence of CA is to multiply the CO_2 hydration rate constants (k_{+1}, a_{+1}, b_{+1}, c_{+1}, k_{-1}, a_{-1}, b_{-1}, and c_{-1}) by a "rate enhancement factor."
5. Isotopic fractionation during mineral growth is described using an ion-by-ion model for calcite (Watkins et al., 2013, 2014; Watkins & Hunt, 2015) but with equilibrium and KFFs appropriate for aragonite (Wang et al., 2013, Section S2 in Supporting Information S1). The model does not include crystal growth via non-classical pathways or possible metastable precursor phases such as amorphous calcium carbonate or other transient $CaCO_3$ phases (Gilbert et al., 2022; Mass et al., 2017; Schmidt et al., 2024; Sun et al., 2020).

3.3. Governing Equations

The differential equations of Chen et al. (2018) that track the isotopic composition of DIC species, alkalinity, and (Ca^{2+}) are:

$$\begin{aligned}\frac{\mathrm{d}[266]}{\mathrm{dt}} = &-k_{+1}[266] + k_{-1}[\mathrm{E2666}]\chi[\mathrm{H}] \\ &-k_{+4}[266][6\mathrm{H}] + k_{-4}[\mathrm{E2666}]\chi \\ &+\frac{D_{\mathrm{cell}}}{z}([266]_{\mathrm{cell}} - [266]) \\ &+\frac{1}{\tau_{\mathrm{sw}}}([266]_{\mathrm{sw}} - [266])\end{aligned} \tag{26}$$

$$\begin{aligned}\frac{\mathrm{d}[366]}{\mathrm{dt}} = &-c_{+1}[366] + c_{-1}[\mathrm{E3666}]^{13}\chi[\mathrm{H}] \\ &-c_{+4}[366][6\mathrm{H}] + c_{-4}[\mathrm{E3666}]^{13}\chi \\ &+\frac{D_{\mathrm{cell}}}{z}([366]_{\mathrm{cell}} - [366]) \\ &+\frac{1}{\tau_{\mathrm{sw}}}([366]_{\mathrm{sw}} - [366])\end{aligned} \tag{27}$$

$$\begin{aligned}\frac{\mathrm{d}[286]}{\mathrm{dt}} = &-b_{+1}[286] + \frac{2}{3}b_{-1}[\mathrm{E2866}]^{18}\chi[\mathrm{H}] \\ &-b_{+4}[286][6\mathrm{H}] + \frac{2}{3}b_{-4}[\mathrm{E2866}]^{18}\chi \\ &+\frac{D_{\mathrm{cell}}}{z}([286]_{\mathrm{cell}} - [286]) \\ &+\frac{1}{\tau_{\mathrm{sw}}}([286]_{\mathrm{sw}} - [286])\end{aligned} \tag{28}$$

$$\begin{aligned}\frac{\mathrm{d}[386]}{\mathrm{dt}} = &-p_{+1}[386] + \frac{1}{3}p_{-1}[\mathrm{E3866}]^{63}\chi[\mathrm{H}] \\ &-s_{+4}[386][6\mathrm{H}] + \frac{2}{3}s_{-4}[\mathrm{E3866}]^{63}\chi \\ &+\frac{D_{\mathrm{cell}}}{z}([386]_{\mathrm{cell}} - [386]) \\ &+\frac{1}{\tau_{\mathrm{sw}}}([386]_{\mathrm{sw}} - [386])\end{aligned} \tag{29}$$

$$\begin{aligned}\frac{\mathrm{d}[288]}{\mathrm{dt}} = &-s'_{+1}[288] + \frac{1}{3}s'_{-1}[\mathrm{E2886}]^{64}\chi[\mathrm{H}] \\ &- s'_{+4}[288][6\mathrm{H}] + \frac{1}{3}s'_{-4}[\mathrm{E2886}]^{64}\chi \\ &+ \frac{D_{\mathrm{cell}}}{z}([288]_{\mathrm{cell}} - [288]) \\ &+ \frac{1}{\tau_{\mathrm{sw}}}([288]_{\mathrm{sw}} - [288])\end{aligned} \tag{30}$$

$$\begin{aligned}\frac{\mathrm{d}[\mathrm{E2666}]}{\mathrm{dt}} = &\, k_{+1}[266] - k_{-1}[\mathrm{E2666}]\chi[\mathrm{H}] \\ &+ k_{+4}[266][6\mathrm{H}] - k_{-4}[\mathrm{E2666}]\chi \\ &+ \frac{1}{\tau_{\mathrm{sw}}}([\mathrm{E2666}]_{\mathrm{sw}} - [\mathrm{E2666}]) \\ &- \frac{F_{\mathrm{CaCO_3}}}{z}\end{aligned} \tag{31}$$

$$\begin{aligned}\frac{\mathrm{d}[\mathrm{E3666}]}{\mathrm{dt}} = &\, c_{+1}[366] - c_{-1}[\mathrm{E3666}]^{13}\chi[\mathrm{H}] \\ &+ c_{+4}[366][6\mathrm{H}] - c_{-4}[\mathrm{E3666}]^{13}\chi \\ &+ \frac{1}{\tau_{\mathrm{sw}}}([\mathrm{E3666}]_{\mathrm{sw}} - [\mathrm{E3666}]) \\ &- \frac{F_{\mathrm{CaCO_3}}}{z}\cdot\frac{[\mathrm{E3666}]}{[\mathrm{E2666}]}\cdot{}^{13}\alpha_{\mathrm{CaCO_3-EIC}}\end{aligned} \tag{32}$$

$$\begin{aligned}\frac{\mathrm{d}[\mathrm{E2866}]}{\mathrm{dt}} = &\, a_{+1}[266]r_{\mathrm{w}} - \frac{1}{3}a_{-1}[\mathrm{E2866}]^{18}\chi[\mathrm{H}] \\ &+ a_{+4}[266][8\mathrm{H}] - \frac{1}{3}a_{-4}[\mathrm{E2866}]^{18}\chi \\ &+ b_{+1}[286] - \frac{2}{3}b_{-1}[\mathrm{E2866}]^{18}\chi[\mathrm{H}] \\ &+ b_{+4}[286][6\mathrm{H}] - \frac{2}{3}b_{-4}[\mathrm{E2866}]^{18}\chi \\ &+ \frac{1}{\tau_{\mathrm{sw}}}([\mathrm{E2866}]_{\mathrm{sw}} - [\mathrm{E2866}]) \\ &- \frac{F_{\mathrm{CaCO_3}}}{z}\cdot\frac{[\mathrm{E2866}]}{[\mathrm{E2666}]}\cdot{}^{18}\alpha_{\mathrm{CaCO_3-EIC}}\end{aligned} \tag{33}$$

$$\begin{aligned}\frac{\mathrm{d}[\mathrm{E3866}]}{\mathrm{dt}} = &\, p_{+1}[366]r_{\mathrm{w}} - \frac{1}{3}p_{-1}[\mathrm{E3866}]^{63}\chi[\mathrm{H}] \\ &+ p_{+4}[266][8\mathrm{H}] - \frac{1}{3}p_{-4}[\mathrm{E3866}]^{63}\chi \\ &+ s_{+1}[386] - \frac{2}{3}s_{-1}[\mathrm{E3866}]^{63}\chi[\mathrm{H}] \\ &+ s_{+4}[386][6\mathrm{H}] - \frac{2}{3}s_{-4}[\mathrm{E3866}]^{63}\chi \\ &+ \frac{1}{\tau_{\mathrm{sw}}}([\mathrm{E3866}]_{\mathrm{sw}} - [\mathrm{E3866}]) \\ &- \frac{F_{\mathrm{CaCO_3}}}{z}\cdot\frac{[\mathrm{E3866}]}{[\mathrm{E2666}]}\cdot{}^{63}\alpha_{\mathrm{CaCO_3-EIC}}\cdot{}^{13}\alpha_{\mathrm{CaCO_3-EIC}}\cdot{}^{18}\alpha_{\mathrm{CaCO_3-EIC}}\end{aligned} \tag{34}$$

$$\begin{aligned}\frac{\mathrm{d}[\mathrm{E2886}]}{\mathrm{dt}} = {} & p'_{+1}\,[286]r_{\mathrm{w}} - \frac{2}{3}p'_{-1}\,[\mathrm{E2886}]^{64}\chi[\mathrm{H}] \\ & + p'_{+4}\,[286][8\mathrm{H}] - \frac{2}{3}p'_{-4}\,[\mathrm{E2886}]^{64}\chi \\ & + s'_{+1}\,[288] - \frac{1}{3}s'_{-1}\,[\mathrm{E2886}]^{64}\chi[\mathrm{H}] \\ & + s'_{+4}\,[288][6\mathrm{H}] - \frac{1}{3}s'_{-4}\,[\mathrm{E2886}]^{64}\chi \\ & + \frac{1}{\tau_{\mathrm{sw}}}\left([\mathrm{E2886}]_{\mathrm{sw}} - [\mathrm{E2886}]\right) \\ & - \frac{F_{\mathrm{CaCO_3}}}{z}\cdot\frac{[\mathrm{E2886}]}{[\mathrm{E2666}]}\cdot {}^{64}\alpha_{\mathrm{CaCO_3-EIC}}\cdot {}^{18}\alpha_{\mathrm{CaCO_3-EIC}}\cdot {}^{18}\alpha_{\mathrm{CaCO_3-EIC}}\end{aligned} \tag{35}$$

$$\begin{aligned}\frac{\mathrm{d}[\mathrm{Ca^{2+}}]}{\mathrm{dt}} = {} & \frac{1}{\tau_{\mathrm{sw}}}\left([\mathrm{Ca^{2+}}]_{\mathrm{sw}} - [\mathrm{Ca^{2+}}]\right) \\ & + \frac{1}{z}\left(\frac{1}{2}f_{\mathrm{Ca}}\,F_{\mathrm{Alk}} - F_{\mathrm{CaCO_3}}\right)\end{aligned} \tag{36}$$

$$\begin{aligned}\frac{\mathrm{d}[\mathrm{Alk}]}{\mathrm{dt}} = {} & \frac{1}{\tau_{\mathrm{sw}}}\left([\mathrm{Alk}]_{\mathrm{sw}} - [\mathrm{Alk}]\right) \\ & + \frac{1}{z}\left(f_{\mathrm{Ca}}\,F_{\mathrm{Alk}} - 2F_{\mathrm{CaCO_3}}\right)\end{aligned} \tag{37}$$

where EIC refers to "equilibrated inorganic carbon" (i.e., HCO_3^- + CO_3^{2-}), χ is the fraction of HCO_3^- in EIC, τ_{sw} (s) is seawater turnover timescale in the CF, $F_{\mathrm{CaCO_3}}$ (mol kg-soln^{-1} s^{-1}) is calcite precipitation flux, F_{Alk} (mol kg-soln^{-1} s^{-1}) is the proton pump rate, z (m) is the thickness of the CF, D_{cell} (m s^{-1}) is the cell permeability of CO_2, f is the fraction of Ca^{2+} of total cations that exchange with H^+ for charge balance, $[CO_2]_{\mathrm{cell}}$ (mol kg-soln^{-1}) is the cellular CO_2 concentration, and the "sw" subscript denotes the concentration of a chemical component in seawater. The $\alpha_{\mathrm{CaCO_3-EIC}}$ terms describe isotope fractionation between $CaCO_3$ and EIC as a function of temperature, pH, and crystal growth rate. Since they are expressed relative to EIC, they depend on both the HCO_3^- and CO_3^{2-} attachment/attachment rates ($k_{\mathrm{B_1}}/k_{\mathrm{B_1}}$ and ${}^{i}k_{\mathrm{B_2}}/k_{\mathrm{B_2}}$ in Table 2).

3.4. Model Implementation

There are five tunable parameters, which are F_{Alk}, D_{cell}, τ_{sw}, the rate enhancement by CA, and the carbon isotope composition of cellular CO_2 (i.e., $[\mathrm{C366}]_{\mathrm{cell}}$). Initially, the CF composition is identical to that of seawater. The Matlab script that accompanies this article is subdivided into the following sequence of operations (pseudocode):

- Specify T, pH, salinity, $[Ca^{2+}]$, [DIC]. These values apply to seawater as well as the initial CF.
- Calculate the equilibrium constants in the DIC-H_2O system (K_1, K_2, K_{w}, and K_{sp}) as functions of T and salinity.
- Calculate DIC speciation from [DIC] and pH (Zeebe & Wolf-Gladrow, 2001).
- Calculate the equilibrium carbon, oxygen, and clumped isotope fractionation factors as functions of T (Table S3 in Supporting Information S1).
- Calculate the forward k values for all reactions.
- Calculate the backward k values using the forward k's and equilibrium constraints.
- Calculate the equilibrium isotopologue concentrations.
- Specify the isotopic composition of intracellular CO_2.
- Solve the system of coupled ODEs (Equations 26–36). At each timestep, the HCO_3^- and CO_3^{2-} isotopologue concentrations are calculated from the EIC isotopologue concentrations using the χ values. These are then used as inputs into the $CaCO_3$-DIC model, which returns the surface area normalized growth rate as well as the pH- and growth rate-dependent ${}^{13}\alpha_{\mathrm{CaCO_3-EIC}}$, ${}^{18}\alpha_{\mathrm{CaCO_3-EIC}}$, ${}^{63}\alpha_{\mathrm{CaCO_3-EIC}}$, and ${}^{64}\alpha_{\mathrm{CaCO_3-EIC}}$ values. The

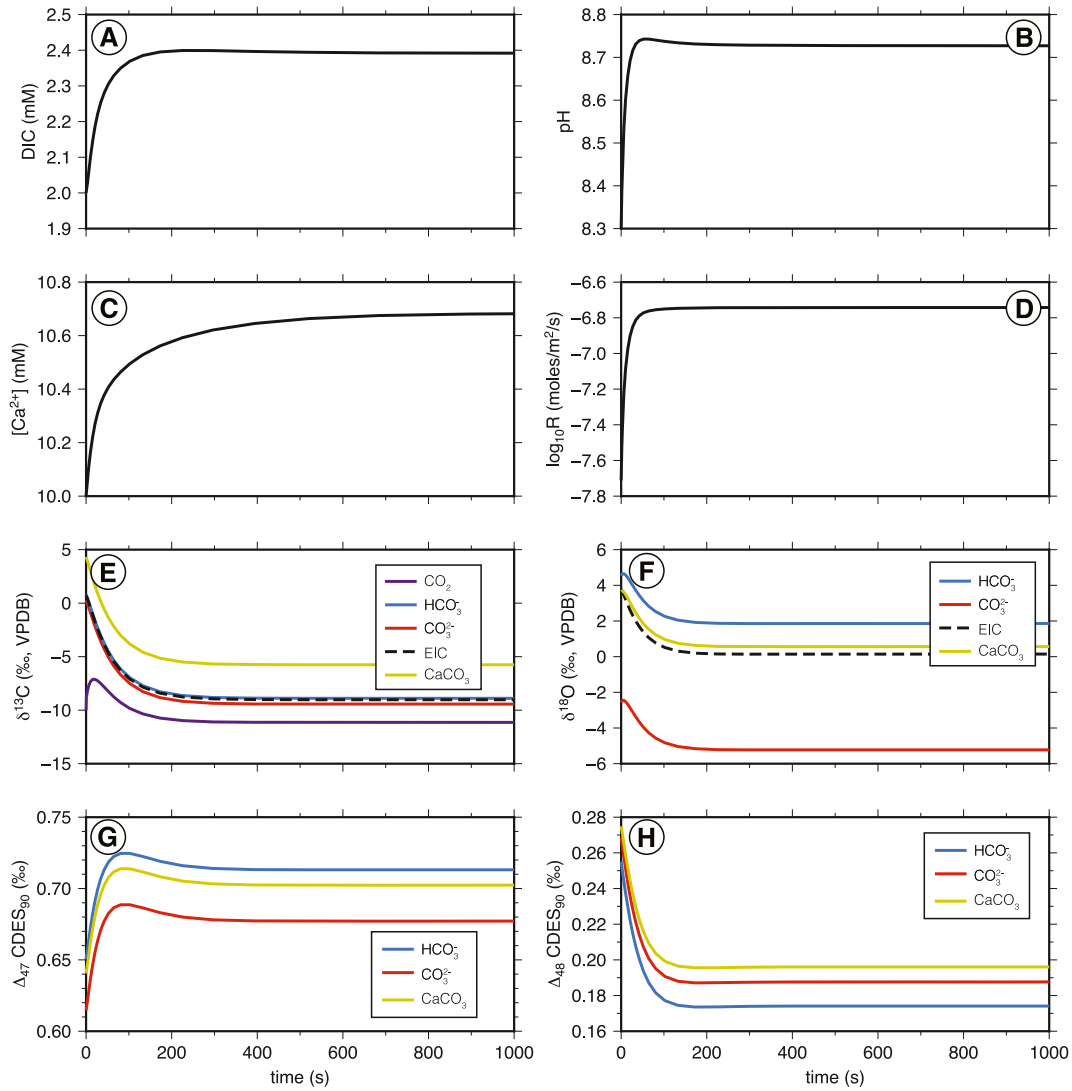

Figure 2. Model outputs for a single run ($F_{Alk} = 0.4 \times 10^{-6}$ moles/m^2/s) showing that the time to reach a steady state isotopic composition is about 200 s. The time to reach steady state does not vary significantly across the range of parameters used in this study. The steady state isotopic composition (panels e–h) can be compared to those shown in Figure 4 for cold-water corals.

calculation is repeated until steady state is reached. A numerical validation of the model is provided in Section S3 in Supporting Information S1.

4. Model Results

4.1. Time to Reach Steady State

An important question is whether corals in nature calcify under steady state conditions. In our simulations, steady state is typically reached within a few minutes (Figure 2), and this result is consistent across a wide range of τ_{sw}, D_{cell}, F_{Alk}, and CA activity. We therefore propose that the composition of the coral CF can be viewed as a sequence of steady states, each potentially shifting in response to longer timescale perturbations such as day-night cycles.

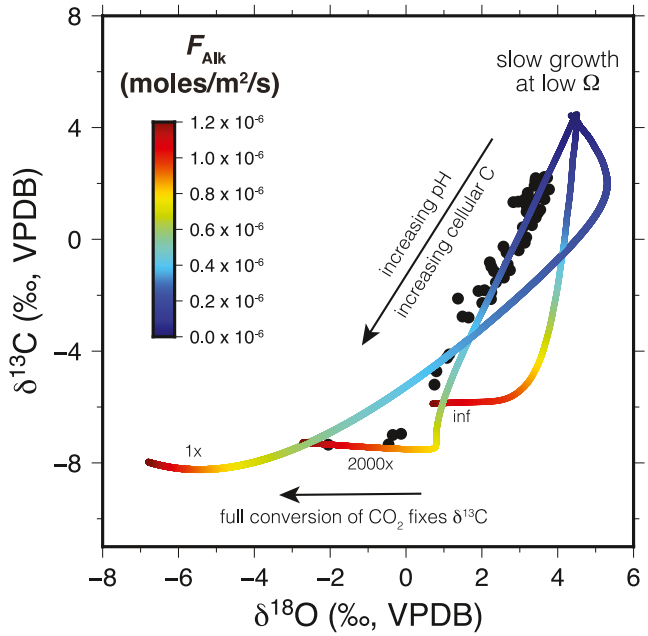

Figure 3. Example from Chen et al. (2018) showing how the coral biocalcification model was used to explain the $\delta^{13}C$-$\delta^{18}O$ data within a single specimen of *Desmophyllum dianthus*. Each point on the curves represents the steady state composition of coral aragonite using parameters provided in Tables 1–3 The curves were generated by varying F_{Alk} while holding all other parameters constant. At low F_{Alk} and [carbonic anhydrase (CA)], the coral grows slowly from a seawater-like calcifying fluid (CF). As F_{Alk} increases, the pH_{cf} increases, which enhances the flux of cellular CO_2 with low $\delta^{13}C$. Upon entering the CF, most of this CO_2 reacts with H_2O (hydration), resulting in ^{18}O-depleted HCO_3^- due to kinetic isotope effects. The $\delta^{13}C$-$\delta^{18}O$ correlation is sensitive to the catalyzing effects of CA on the CO_2 hydration reaction, and a rate enhancement factor of about 2,000x is consistent with the data (Chen et al., 2018).

4.2. Intra-Coral $\delta^{13}C$-$\delta^{18}O$ Variations

For data-model comparison, we take the approach of Chen et al. (2018) and re-fit the $\delta^{13}C$-$\delta^{18}O$ trends within one of their deep-sea corals by varying F_{Alk} while holding all other parameters constant (Figure 3). This serves the purposes of introducing the model outputs and demonstrating that previous conclusions remain valid despite changes to some of the input constants (Table 2). Figure 3 shows how steady state coral compositions compare to data from the specimen of deep-sea coral *D. dianthus* (Adkins et al., 2003). At low F_{Alk}, the model coral grows at low supersaturation from a CF that resembles seawater. As F_{Alk} increases, protons are pumped out of the CF, which elevates pH_{cf} and enhances the cellular CO_2 flux. The pH up-regulation increases the KIEs attending CO_2 hydration and hydroxylation by making these reactions more unidirectional. The minimum in $\delta^{13}C$ is reached when the seawater contribution of carbon to the CF is small compared to the cellular contribution, at which point the incoming cellular CO_2 gets (nearly) quantitatively converted to HCO_3^-. This fixes the $\delta^{13}C$ but not the $\delta^{18}O$ of EIC because of the additional contribution of oxygen from H_2O and/or OH^-. The $\delta^{18}O$ of EIC can continue to get isotopically lighter with increasing F_{Alk} as the hydration and hydroxylation reactions become increasingly unidirectional. As noted by Chen et al. (2018), the $\delta^{13}C$-$\delta^{18}O$ slope is sensitive to CA activity, and a rate enhancement of about 2,000x yields model results that are consistent with the data.

4.3. Inter-Coral $\delta^{13}C$-$\delta^{18}O$ and Δ_{47}-Δ_{48} Variations

By varying F_{Alk} with our model, we can also reproduce the observed *inter*-species variations in $\delta^{13}C$ and $\delta^{18}O$ (Figure 4a). As a group, the deep-sea corals display a $\delta^{13}C$-$\delta^{18}O$ covariation that is strikingly similar to those observed within the single specimen of *D. dianthus* (Figure 3) and consistent with a 2,000x rate enhancement. By contrast, CA activity is essentially unconstrained by the more scattered $\delta^{13}C$-$\delta^{18}O$ data of the tropical coral group. The tropical corals also require a contribution of ^{13}C-enriched metabolic CO_2 to shift the model curves upwards by +5‰ so that they pass through the data cloud. For both groups of corals, different combinations of D_{cell} and τ_{sw} can yield similar fits to the data, as discussed further below.

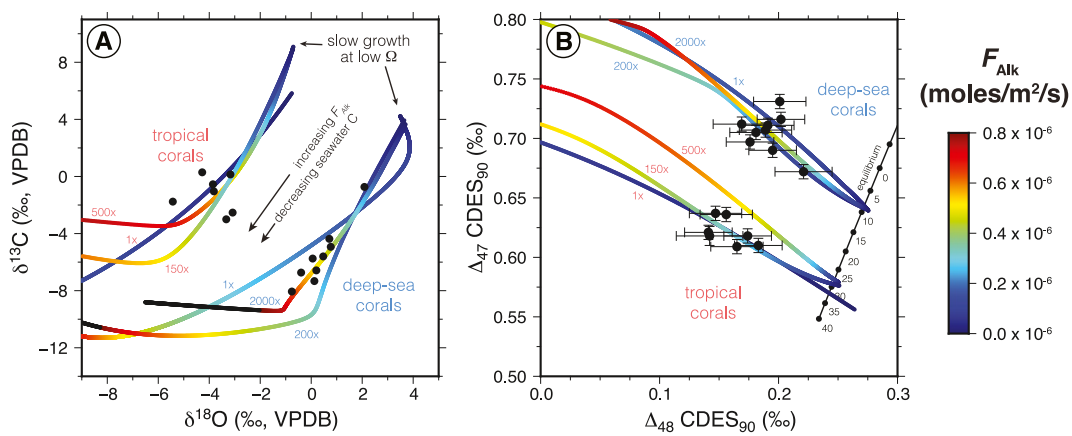

Figure 4. Coral biocalcification model outputs compared to inter-species variability. The model can simultaneously fit (a) the $\delta^{13}C$-$\delta^{18}O$ data and (b) the Δ_{47}-Δ_{48} data using a single set of parameters. The τ_{sw} and D_{cell} values used to construct these curves are provided in Table 3, and a different set applies to tropical versus deep-sea corals. The labels on the curves refer to the CO_2 hydration rate enhancement by carbonic anhydrase activity, which is greater for deep-sea corals (2,000x) than for tropical corals (<500x), as constrained by using both the $\delta^{13}C$-$\delta^{18}O$ and Δ_{47}-Δ_{48} data.

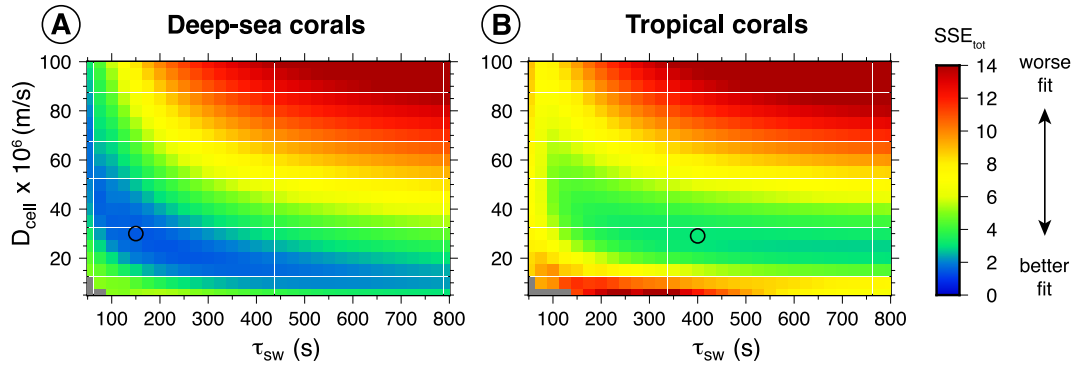

Figure 5. Color maps showing how the goodness-of-fit (SSE_{tot}) varies for different combinations of D_{cell} and τ_{sw}. The model can achieve a lower SSE_{tot} for the deep-sea corals (a) than for the tropical corals (b) because of the stronger $\delta^{13}C$-$\delta^{18}O$ co-variation exhibited by the deep-sea corals. For both data sets, there is not a unique combination of D_{cell} and τ_{sw} that yields a best fit, but rather, a range of values that yield a similarly low SSE_{tot}. Overall, the data from deep-sea corals suggest a lower τ_{sw} than for tropical corals, which implies greater fractional contribution of cellular CO_2 to the DIC budget of the calcifying fluid for deep-sea corals. Black circles show the parameters used in the construction of Figures 8 and 9.

The new dual clumped isotope data offer additional constraints without the penalty of introducing new parameters (Figure 4b). A key result is that a single set of parameters can simultaneously fit the $\delta^{13}C$-$\delta^{18}O$ and Δ_{47}-Δ_{48} data for each group of corals. The Δ_{47}-Δ_{48} data for tropical corals is consistent with a CA rate enhancement factor between 1 and 500x, or roughly an order of magnitude lower than for deep-sea corals.

4.4. Finding the Best-Fit Parameters

We performed sensitivity runs to constrain the $\delta^{13}C$ metabolic CO_2 shift and CA rate enhancement factor for each group of corals. Then, with those parameters established, there are different combinations of τ_{sw} and D_{cell} that can fit all four isotopic measurements simultaneously (Section S4 in Supporting Information S1). To constrain τ_{sw} and D_{cell} objectively, we calculated the sum of square error (SSE_{tot}) for different combinations. The results are displayed graphically in Figure 5. For both data sets, the minimum in SSE_{tot} spans a range of values, but overall, we find that deep-sea corals are better fit by some combination of lower τ_{sw} and/or higher D_{cell} than for tropical corals. In subsequent figures, we set a distinct τ_{sw} for deep-sea corals (150 s) versus tropical corals (400 s) and assume a constant $D_{cell} = 30 \times 10^{-6}$ m/s for all corals.

5. Discussion

5.1. Origin of KIEs in $\delta^{13}C$-$\delta^{18}O$ and Δ_{47}-Δ_{48} Space

The carbon and oxygen KIEs within and among corals are due mainly to the CO_2 hydration reaction (Chen et al., 2018; Devriendt et al., 2017). While the isotopic fractionations attending the crystal growth reactions are comparatively minor (~1–2‰ for $\delta^{13}C$ and $\delta^{18}O$), it is important to include the crystal growth terms because the kinetics of crystal growth influence the reversibilities of the CO_2 hydration and hydroxylation reactions (Watkins & Devriendt, 2022).

Although CO_2 hydration is the dominant source of KIEs in corals, we graphically display the effects of other kinetic processes on the isotopic signatures of corals with vectors (Figure 6a). Vectors are plotted with similar lengths for illustrative purposes only and do not represent the actual influence of different KIEs on corals. For this exercise, we use the deep-sea corals as an example but note that the trajectories of the different processes vary with temperature and parameter set. For $\delta^{13}C$-$\delta^{18}O$, the decomposition is similar to that of Chen et al. (2018) (see their Figure 7) but our hydration slope is steeper because we use a smaller oxygen isotope KFF (b_{+1}/k_{+1}) and larger carbon isotope KFF (c_{+1}/k_{+1}) (Table 2; Section S5 in Supporting Information S1). A feature highlighted by Chen et al. (2018) is that the $\delta^{13}C$-$\delta^{18}O$ slope increases monotonically with increasing CA rate enhancement. We find, however, that our steeper hydration slope leads to a more complicated relationship with CA activity whereby the overall $\delta^{13}C$-$\delta^{18}O$ slope is steeper for the 200x case than for the 2,000x case (Figure 4a). The original behavior from Chen et al. (2018) is recovered when their KFFs are used.

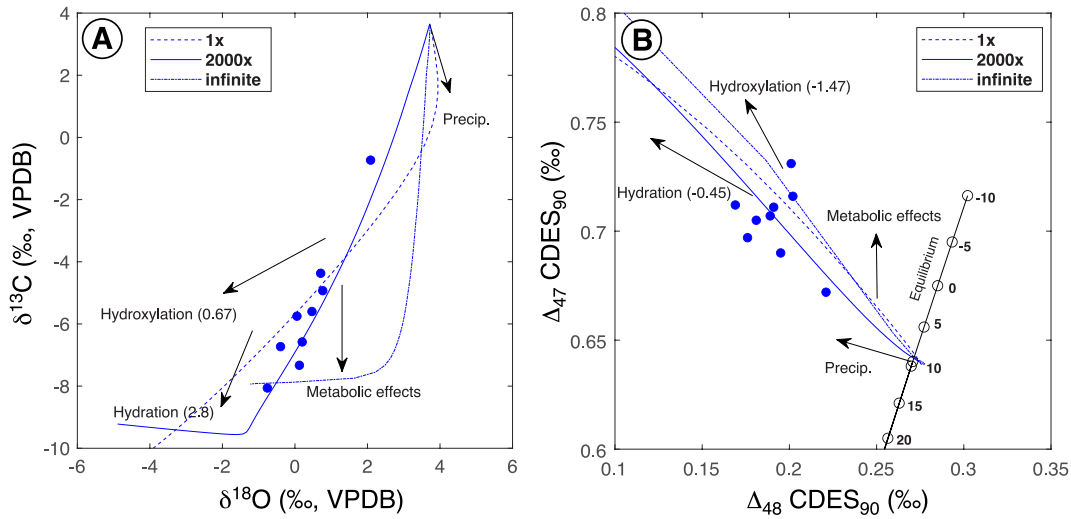

Figure 6. Vectors showing the effects of various processes on (a) $\delta^{13}C$-$\delta^{18}O$ and (b) Δ_{47}-Δ_{48}. Numbers in parentheses denote the slope. Blue curves show the effect of varying the CO_2 hydration rate enhancement factor. *Hydration vector*: Under low F_{Alk} conditions, which results in a low pH_{cf}, we compare the results using a finite rate enhancement factor with those obtained using an infinite rate enhancement factor (DIC-H_2O equilibrium). *Hydroxylation vector*: Same as hydration vector but with high F_{Alk}. *Metabolism vector*: While keeping all other parameters constant, we find that a decrease in the $\delta^{13}C$ of $CO_{2,cell}$ leads to a decrease in $\delta^{13}C$ and increase in Δ_{47} while $\delta^{18}O$ and Δ_{48} remain unchanged. *Precipitation vector*: We compare results with and without kinetic isotope effects attending the crystal growth reactions. All other vectors are plotted assuming no kinetic fractionation during precipitation.

The Δ_{47}-Δ_{48} patterns can also be decomposed (Figure 6b) following the same approach, providing insight as to why the Δ_{47}-Δ_{48} slope is relatively insensitive to DIC-H_2O kinetics. Consider, for example, the 1x versus instantaneous kinetics scenarios. In the instantaneous case, the coral can take full advantage of the cross-membrane CO_2 source, leading to a near-vertical $\delta^{13}C$-$\delta^{18}O$ slope that aligns with the metabolic trajectory and reflects carbon source mixing. By contrast, the same scenario shifts the Δ_{47}-Δ_{48} curve only slightly toward the metabolic trajectory because mixing between isotopically distinct carbon sources leads to muted effects in clumped isotope space (Defliese & Lohmann, 2015).

5.2. Comparison to IsoDIC Model

Davies et al. (2022) used the IsoDIC model of Guo (2020) to interpret their Δ_{47}-Δ_{48} data. The IsoDIC model differs from the COAD model presented here in several ways. IsoDIC is solely based on DIC-H_2O reaction kinetics (Figure 7a) and does not include the effect of aragonite precipitation on the kinetics of CO_2 hydration and hydroxylation. Moreover, IsoDIC outputs reflect transient states from equilibrium to a return to equilibrium following a perturbation of the system by the input of a CO_2 source. In contrast, COAD outputs reflect steady states in the full $CaCO_3$-DIC-H_2O system. We argue that a coral CF is likely to reach steady state since it is achieved within 2–3 min in our model simulations following activation of the alkalinity pump (Section 4.1).

This conceptual difference between the two models significantly impacts the KIE "trajectories" (Figure 4 vs. Figure 7). Although both IsoDIC and our COAD model reproduce the Δ_{47}-Δ_{48} data, only the COAD model reproduces all isotopic measurements ($\delta^{13}C$, $\delta^{18}O$, Δ_{47}, and Δ_{48}) with a unique set of parameters. Importantly, the interspecimen variability in $\delta^{13}C$-$\delta^{18}O$ and Δ_{47}-Δ_{48} are explained differently by the two models. IsoDIC suggests $\delta^{13}C$-$\delta^{18}O$ variations are caused by aragonite precipitating at different times during an equilibrium-disequilibrium cycle (i.e., transient state, Figure 7b), while Δ_{47}-Δ_{48} variations are caused by the "time" effect as well as significant variations in CA activities (Figure 7c). In contrast, COAD involves distinct proton pump activities (i.e., different F_{Alk}) as the main cause of both $\delta^{13}C$-$\delta^{18}O$ and Δ_{47}-Δ_{48} covariations (Figure 4). Hence, the COAD model invokes a single physiologic mechanism (i.e., proton pump activity) to explain most of the variation in all four isotopic measurements, while IsoDIC requires distinct mechanisms and parameter values to reproduce the $\delta^{13}C$-$\delta^{18}O$ and Δ_{47}-Δ_{48} covariations. Last, the COAD model predicts significantly higher CA activities in coral

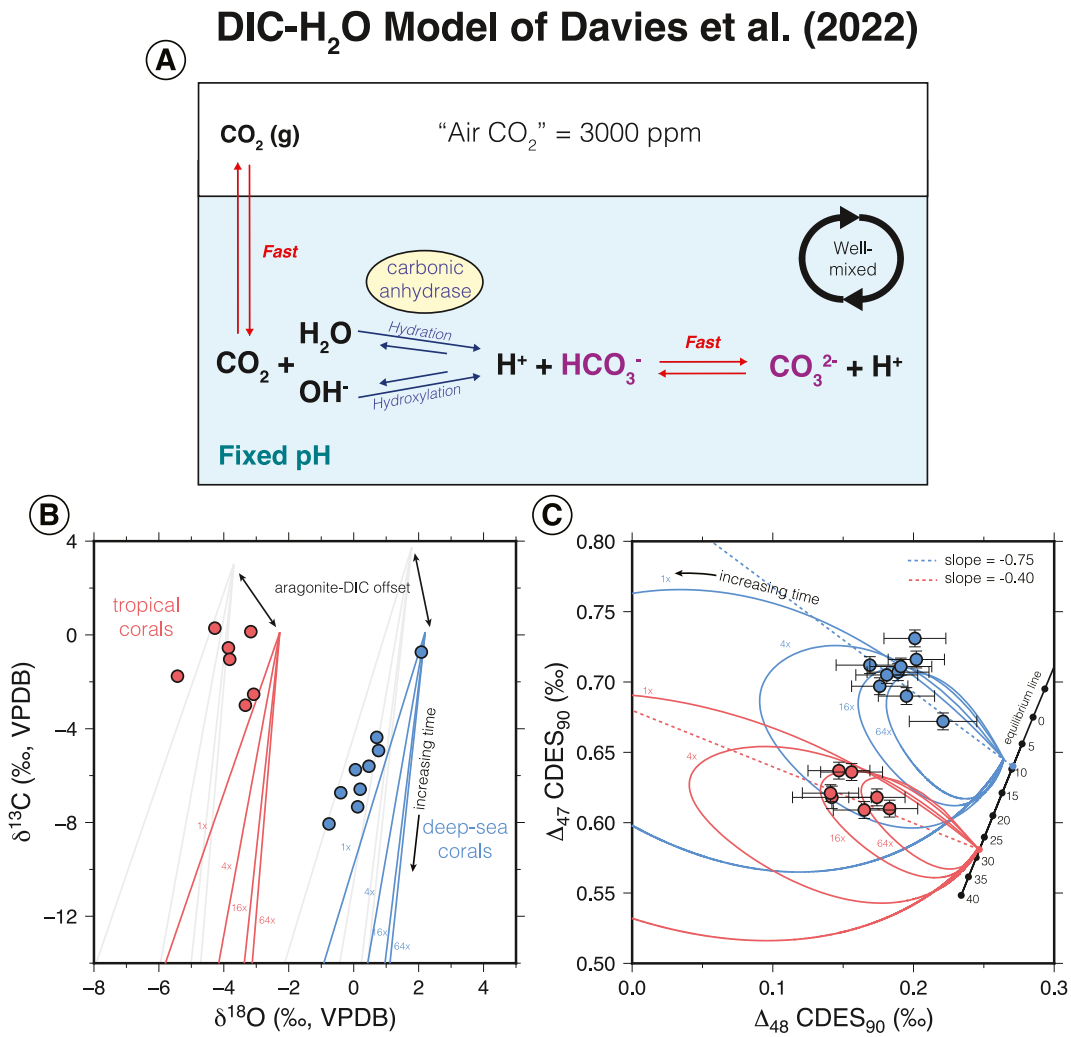

Figure 7. (a) Schematic of the IsoDIC model of Guo (2020) as applied to corals in Davies et al. (2022). (b) Stable isotope composition of EIC for warm corals (red) and cold corals (blue). Curves show IsoDIC outputs for different values of the rate enhancement factor (1x to 64x). Gray curves represent the composition of aragonite assuming a constant offset from EIC. (c) Dual-clumped isotope composition of EIC for tropical and deep-sea corals. The equilibrium line is for aragonite, which is offset slightly from the equilibrium composition of EIC (Hill et al., 2020). Loops start and end at the equilibrium EIC composition and represent outputs for different values of the rate enhancement factor (1x to 64x). Dashed lines represent the empirical slopes used in Figure 8a.

CFs relative to the IsoDIC model. IsoDIC suggests CO_2 rate enhancement factors from 1x to 8x for deep-sea corals and 4x to 30x for tropical corals, while COAD predicts factors of 2,000x for deep-sea corals and up to 500x for tropical corals.

5.3. Dual Clumped Isotope Thermometry

Dual clumped thermometry is a new approach for extracting temperatures from carbonate samples that were previously thought to be compromised by kinetic effects (Bajnai et al., 2020; Guo, 2020; Guo & Zhou, 2019). The premise is that a given kinetic process (e.g., CO_2 degassing or CO_2 absorption) leads to correlated KIEs in Δ_{47}-Δ_{48} space, and if the correlation slope is known, the true temperature of a sample can be retrieved. Davies et al. (2022) took this approach and proposed slopes of −0.75 and −0.40 for deep-sea and tropical corals, respectively (Figure 8a). Since these slopes are empirical, it remains an open question why the tropical corals exhibit a shallower slope.

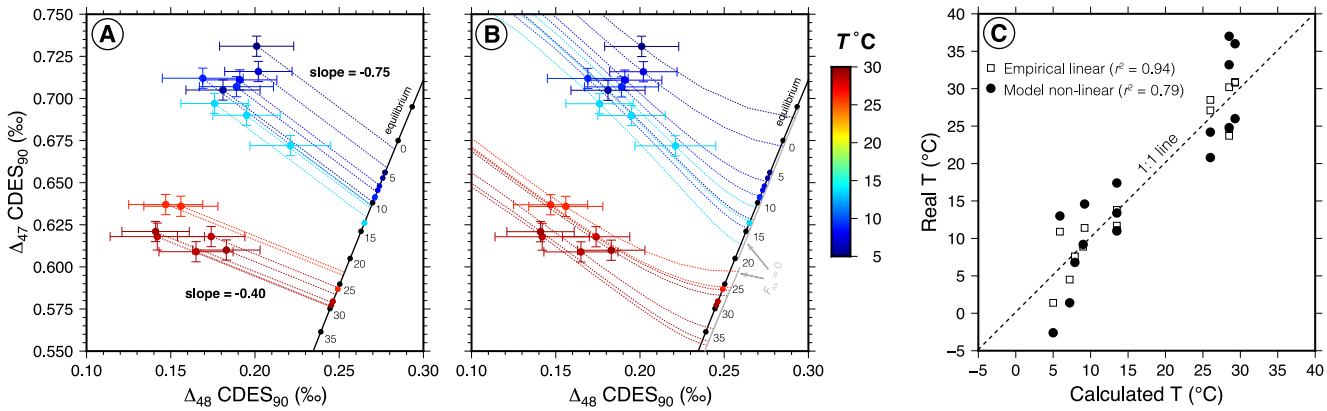

Figure 8. Methods for retrieving temperatures from samples that deviate from the equilibrium line. (a) Linear projections to the equilibrium line using empirical slopes of −0.40 and −0.75 for warm and cold water corals, respectively (Davies et al., 2022). (b) Model-derived, non-linear projections to the $F_{Alk} = 0$ line (this study). The $F_{Alk} = 0$ line is offset from the equilibrium line because even in the absence of an alkalinity pump, the processes of seawater flushing, CO_2 diffusion and aragonite precipitation proceed, resulting in a steady state where the composition of the calcifying fluid is slightly different from that of seawater. The larger offset between the "$F_{Alk} = 0$" and equilibrium lines for warm-water corals is due to lower carbonic anhydrase rate enhancement. (c) The empirical linear corrections perform slightly better than the model non-linear corrections for kinetic effects in the case where the model parameters are assumed to be constant and applicable to different coral species within the tropical and deep-sea coral groups.

The coral biocalcification model can offer insights. To back-project the Δ_{47}-Δ_{48} data to the equilibrium line, we start by assuming the values of $\delta^{13}C_{CO_2,cell}$, CA activity, τ_{sw} and D_{cell} in Table 3 are "correct" and applicable to multiple species of coral even though they were optimized to pass through the data clusters as a whole. Then, we vary the model temperature until the model-derived curve passes through a given data point and determine the temperature corresponding to $F_{Alk} = 0$, as shown in Figure 8b. The empirical and model-derived temperatures are compared in Figure 8c. Both yield similar results but the empirical approach performs better for this data set ($r^2 = 0.94$ vs. 0.79). This is not surprising given the constraints imposed on the model, which could be relaxed (e.g., by parsing the data by species) but at the expense of additional tunable parameters.

According to the model, the shallower slope for tropical corals is attributable to a combination of lower CA activity and reduced flushing of the CF with seawater (i.e., higher τ_{sw} and/or D_{cell}) relative to deep-sea corals. We speculate that deep-sea corals require higher CA activity to compensate for the slower kinetics of CO_2 hydration at lower temperatures. Tropical corals, on the other hand, may be better adapted to restrict seawater exchange with the CF, potentially as an evolutionary response to greater salinity and pH variability driven by mixing with meteoric or riverine freshwater.

5.4. Biomineralization Processes

The carbon, oxygen and clumped isotope disequilibrium signatures of coral aragonite were simultaneously reproduced within a single process-based framework for coral calcification and isotopic fractionation. This framework allowed the quantification of critical parameters controlling aragonite formation, including the carbon sources (seawater DIC, cellular CO_2), the chemical state of the CF (pH_{cf}, Ω_{arag}, $[CO_3^{2-}]$, $[Ca^{2+}]$, [CA], reversibility of reactions) and the aragonite growth rate. Model coral parameters were inferred from a best-fit approach to all four aragonite isotopic values ($\delta^{13}C$-$\delta^{18}O$-Δ_{47}-Δ_{48}, Table 3). Where available, these model-derived

Table 3
Biological Model Parameters

Data	D_{cell} (m/s)	τ_{sw} (s)	CA rate enhancement	$\delta^{13}C_{CO_2}$ offset
Cold - Chen et al. (2018)	25×10^{-6}	120	~2,000x	0‰
Cold - Davies et al. (2022)	30×10^{-6}	150	~2,000x	−1‰
Warm - Davies et al. (2022)	30×10^{-6}	400	~150x	+5‰

variables are compared to published *in-situ* measurements of the CF carbonate chemistry and to δ^{11}B-derived pH_{cf} values and B/Ca-derived $[CO_3^{2-}]_{cf}$.

5.4.1. pH_{cf}

Modeled coral pH_{cf} values are all higher than typical seawater pH ($pH_{T,sw} = 8.05 \pm 0.05$, total scale, Jiang et al., 2019), ranging from 8.4 to 9.3 for deep-sea corals and 8.2 to 8.4 for tropical corals (Figures 9a and 9b). An elevated coral pH_{cf} relative to pH_{sw} is consistent with previously reported pH_{cf} for corals grown in the field (McCulloch et al., 2012; Trotter et al., 2011) and in aquariums with natural seawater (Krief et al., 2010; Trotter et al., 2011; Venn et al., 2011). To facilitate the comparison of pH_{cf} values obtained from different studies, methods and environments, we use the ΔpH notation ($\Delta pH = pH_{cf} - pH_{sw}$).

For tropical corals, our model results indicate a narrow ΔpH range from 0.11 to 0.25. The ΔpH of tropical corals has previously been estimated using three different methods. Microelectrodes inserted in the CF of cultured *Stylophora* corals provide the most direct and precise pH_{cf} measurements to date, with a reported ΔpH average of 0.44 ± 0.10 (1 SD, $n_{coral} = 12$; Sevilgen et al., 2019), which is higher than our modeled ΔpH. Measurements of pH_{cf} via microelectrodes carried out prior to the study of Sevilgen et al. (2019) are not discussed here because of a lack of visual controls and concerns over potential disruptions of polyp biological activity during the measurements (cf. Sevilgen et al., 2019). Another direct method of pH_{cf} measurement uses the pH-sensitive dye SNARF-1 on thin layers of corals growing on glass slides (e.g., Allison et al., 2023; Holcomb et al., 2014; Sevilgen et al., 2019; Venn et al., 2011, 2013). For *Stylophora, Pocillopora* and *Acropora sp.* grown in aquaria with natural seawater pH and [DIC], these studies reported ΔpH ranging from 0.12 to 0.69 during daylight and 0.07 to 0.36 in the dark (Allison et al., 2023; Comeau et al., 2017; Venn et al., 2011, 2019, 2022). Taking the average ΔpH for light and dark conditions for all corals yields $\Delta pH_{average} = 0.21 \pm 0.09$ (1 SD, ncoral = 8) for the SNARF-1 method, which is very close to our modeled value. The aragonitic skeletons of hundreds of tropical corals from the field have been analyzed for δ^{11}B (e.g., Allison et al., 2023; Canesi et al., 2023; Krief et al., 2010; McCulloch et al., 2012, 2017; Trotter et al., 2011), including the genus *Porites* and *Acropora sp.*, which are reported in this study. No taxonomic effects on δ^{11}B were recorded for these two genera, leading to a pooled $\Delta pH_{average}$ of 0.40 ± 0.06 ($n_{coral} = 41$; McCulloch et al., 2017; Ross et al., 2022; Canesi et al., 2023, 2024). Therefore, our modeled $\Delta pH_{average}$ for tropical corals agrees best with the SNARF-1 ΔpH estimation and is slightly lower than estimations from the microelectrode and δ^{11}B studies.

For deep-sea corals, our model results indicate a comparatively higher and more variable ΔpH ranging from 0.55 to 0.80. The pH_{cf} of deep-sea corals has not been measured with a direct method (microelectrode or SNARF-1) to date but indirect estimations using the δ^{11}B proxy yield ΔpH ranging from 0.31 to 1.07 ($\Delta pH_{average} = 0.80 \pm 0.16$, 1 SD, ncoral = 21; McCulloch et al., 2012), in excellent agreement with our findings.

Overall, our modeled coral ΔpH are in good agreement with estimates from other methods, capturing the higher and more variable ΔpH for deep-sea corals than for tropical corals. More direct comparisons and evaluation of the clumped isotope results may be achieved in future studies by pairing clumped isotopes with another method of pH_{cf} determination on the same coral samples (e.g., $\delta^{13}C$-$\delta^{18}O$-Δ_{47}-Δ_{48} with δ^{11}B).

5.4.2. $[CO_3^{2-}]_{cf}$

For tropical corals, modeled $[CO_3^{2-}]_{cf}$ (~270 ± 20 μM, $n_{coral} = 7$) are comparable to seawater values. This contrasts with significantly higher $[CO_3^{2-}]_{cf}$ obtained by inserting a microelectrode in the CF of cultured *Stylophora* ($[CO_3^{2-}]_{cf} = 700 \pm 200$ μM, $n_{coral} = 10$; Sevilgen et al., 2019). Estimates based on aragonite B/Ca of field corals suggest even higher $[CO_3^{2-}]_{cf}$ of ~$1{,}140 \pm 100$ μM (1 SD, $n_{coral} = 47$; McCulloch et al., 2017; Ross et al., 2022; Canesi et al., 2023, 2024). Our modeled tropical coral $[CO_3^{2-}]_{cf}$ are therefore likely to be underestimated. This discrepancy is mostly explained by a lower modeled $[DIC]_{cf}$ (1.6 ± 0.1 mM) since pH_{cf} estimations are in good agreement (Section 5.4.1). We hypothesize that our model may be missing an additional source of DIC_{cf}, such as active HCO_3^- transport. A range of bicarbonate transporters identified in stony corals but absent in non-skeleton-forming relatives suggest active HCO_3^- transport may be critical to coral calcification (Tinoco et al., 2023; Vidal-Dupiol et al., 2013; Zoccola et al., 2015). Genetic editing of the Na^+-coupled HCO_3^- transporter SLC4γ in stony corals resulted in poor calcification (Tinoco et al., 2023), further supporting the role of

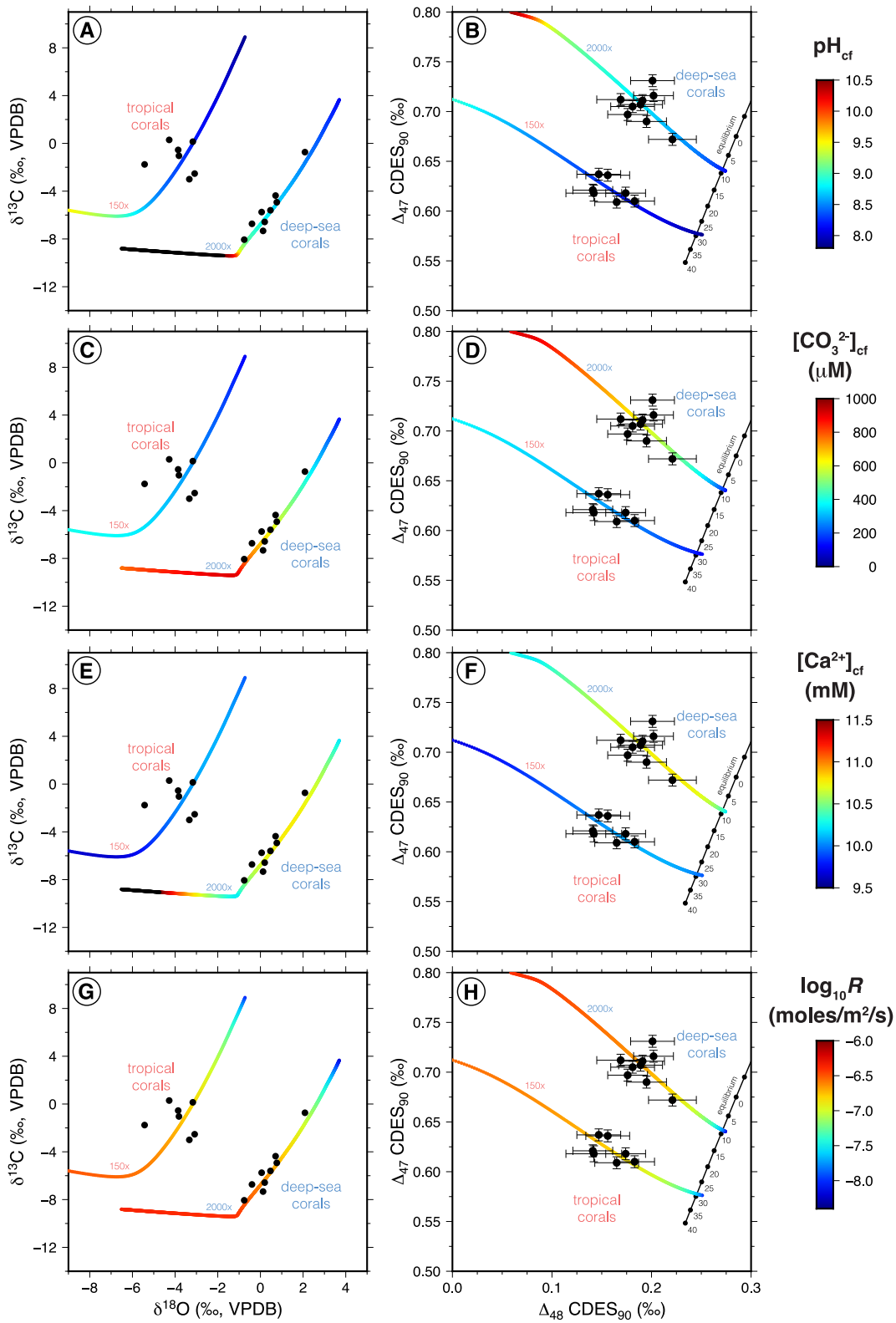

Figure 9. Curves color-coded by different model outputs. (a)–(f) Modeled composition of the calcifying fluid. (g)–(h) Modeled aragonite growth rate.

HCO_3^- transporter in skeleton formation. An active HCO_3^- transporter was not part of the Chen et al. (2018) model and we have not added it yet because it is not necessary to explain the new dual clumped isotopic data. However, we recognize that such transporters may play a critical role in calcification and the modulation of the CF carbonate chemistry.

For deep-sea corals, modeled $[CO_3^{2-}]_{cf}$ are significantly higher than for tropical corals (~600 ± 75 μM). To the best of our knowledge $[CO_3^{2-}]_{cf}$ has not been measured directly in deep-sea corals but was estimated from B/Ca measurements (Fietzke & Wall, 2022). The B/Ca results indicate spatially variable B concentration in *D. pertusum* with zones of high and low B/Ca values. Low B/Ca values correspond to early mineralization zones while higher B/Ca values are from the fibrous part of the coral skeleton. Converting the B/Ca values of the fibrous part, which largely dominate the aragonite budget of corals (Cuif & Dauphin, 2005), yields $[CO_3^{2-}]_{cf}$ of 500–800 μmol/kg, in good agreement with our modeled $[CO_3^{2-}]_{cf}$.

5.4.3. $[Ca^{2+}]_{cf}$

Our modeled $[Ca^{2+}]_{cf}$ for tropical (10.1 ± 0.1 mM) and deep-sea (10.7 ± 0.1 mM) corals (Figures 9e and 9f) are close to the seawater value (10.3 mM). $[Ca^{2+}]_{cf}$ was measured directly with a microelectrode in six cultured colonies of the tropical coral *Stylophora pistillata* (Sevilgen et al., 2019) and yielded time averaged $[Ca^{2+}]_{cf}$ in light and dark ranging from 11 (their seawater value) to 15.5 mM ($[Ca^{2+}]_{cf,\ average} = 13.0 \pm 2.0$ mM). It is unclear at this stage if the modestly higher $[Ca^{2+}]_{cf}$ results from Sevilgen et al. (2019) can be extrapolated to other corals and environments or are specific to their culture experiment. Overall, our modeled results agree with the microelectrode results insofar as they suggest $[Ca^{2+}]_{cf}$ is similar to or slightly higher than $[Ca^{2+}]_{sw}$ due to alkalinity pumping.

5.4.4. CA Activity in Corals

The activity of CA normalized to the polyp tissue volume was found to be ~50 s^{-1} for *Porites* and ~400 s^{-1} for *Siderastrea* (Hopkinson et al., 2015). In their experiment, the CO_2 hydration background rate (i.e., in the absence of CA) was ~0.15 s^{-1}, suggesting a CA rate enhancement factor of ~330x for the *Porites* specimen and ~2,700x for the *Siderastrea* specimen. For tropical corals, our model fits the isotopic data with a CA rate enhancement factor below 500x, which is compatible with the Hopkinson et al. (2015) results for *Porites* but not with *Siderastrea*. We note, however, that the experimental determination of CA activity was carried out on bulk polyp tissues and does not differentiate between cellular CA and CF CA. To the best of our knowledge, CA activity has not been measured in deep-sea coral tissues but our model results suggest higher CA rate enhancement factors (~2,000x) than for tropical corals.

5.4.5. Aragonite Growth Rate

Modeled aragonite growth rates range from $\log_{10}R = -6.9$ to -6.6 mol/m^2/s (Figures 9g and 9h). Robinson et al. (2014) compiled linear growth rates (expressed in mm yr^{-1}) for aragonitic scleractinian coral species, which span over three orders of magnitude, from <0.01 to ~25 mm yr^{-1}. The linear growth rates can be converted to surface area normalized growth rates (moles/m^2/s) using the molecular weight of aragonite (100.087 g mol^{-1}) and coral density (g cm^{-3}), the latter being dependent on porosity. As porosity decreases, bulk density approaches micro-density, neither of which should exceed the specific gravity of aragonite (2.94 g cm^{-3}). A compilation of bulk densities and micro-densities provide lower and upper bounds of 0.8 and 2.9 g cm^{-3}, respectively (Bucher et al., 1998). Using these values, the range of measured surface area-normalized growth rates is $\log_{10}R = -8.6$ to -4.6 mol m^{-2} s^{-1}. The slow growth endmember is consistent with corals grown from a seawater-like fluid (i.e., $F_{Alk} = 0$) and our expectation is that such corals (e.g., *Enallopsammia rostrata*) would have near-equilibrium Δ_{47} and Δ_{48} values (Figure 9h). The corals analyzed by Davies et al. (2022) suggest growth rates near the middle of the natural range. The model growth rates plateau at $\log_{10}R \approx -6.6$ (Section S3 in Supporting Information S1), making it difficult to explain corals whose growth rates exceed this value. As discussed above, our modeled $[CO_3^{2-}]_{cf}$ values for tropical corals are low, suggesting that another source of DIC may be missing from the model, which might be necessary to reconcile the fast growth rates exhibited by some corals with the fast growth limit of the model.

6. Summary and Conclusions

Corals are anomalous among the various marine biocalcifying organisms in that they display some of the largest "vital effects," or biologically mediated deviations from isotopic equilibrium. While vital effects complicate the use of corals for paleoclimate reconstructions, they offer a window into biomineralization processes. We updated and expanded a process-based coral biomineralization model and applied it to new dual-clumped isotope data (Δ_{47} and Δ_{48}) from deep-sea and tropical corals. The key findings are:

1. Deviations from dual clumped isotope equilibrium are due primarily to the CO_2 hydration reaction, the reversibility of which is modulated by the activity of CA, the strength of the biological proton pump, and the kinetics of calcification.
2. The model cannot reproduce the bulk of the isotopic data without the catalytic effect of CA on the CO_2 hydration reaction rate in the coral CF. Optimal data-model agreement for both $\delta^{13}C$-$\delta^{18}O$ and Δ_{47}-Δ_{48} is achieved where the CO_2 hydration reaction rate is increased by ∼2,000x for deep-sea corals and by 1–500x for tropical corals. The latter compares well with the reaction enhancement measured in the tissues of tropical species.
3. The Δ_{47}-Δ_{48} slope is sensitive to the cell permeability of CO_2 (D_{cell}) and seawater residence time in the CF (τ_{sw}). Higher D_{cell} and/or τ_{sw} can explain the shallower Δ_{47}-Δ_{48} slope exhibited by tropical corals. This implies a greater contribution of the cellular CO_2 flux relative to the seawater DIC flux for tropical versus deep-sea corals.
4. The modeled compositions of the CF (pH_{cf} $[Ca^{2+}]_{cf}$, and $[CO_3^{2-}]_{cf}$) are in good overall agreement with in situ measurements and other indirect techniques. Underestimates in the modeled $[Ca^{2+}]_{cf}$, and $[CO_3^{2-}]_{cf}$ could be due to Ca^{2+} and/or HCO_3^- transport through ion-selective channels. Such an additional source of Ca^{2+} and/or DIC may be necessary to explain natural coral growth rates that exceed the maximum model values ($\log_{10}R \approx -6.6$ mol/m^2/s). It is also possible that the growth law for inorganic aragonite is not be suitable for some corals, especially in light of recent evidence for coral growth by non-classical pathways.

In summary, the data-model agreement is encouraging and constitutes meaningful progress toward a quantitative version of a general biocalcification model that may be adaptable to a variety of calcifying organisms.

Data Availability Statement

Matlab scripts for the model presented herein are available on GitHub (https://github.com/jwatkins529/COAD_Box_Model_Coral) and Zenodo (Watkins, 2025).

Acknowledgments
We gratefully acknowledge the constructive reviews by Casey Saenger and Jamie Lucarelli, which significantly improved the clarity of the manuscript, particularly in regards to distinctions between steady state and transient modeling approaches. Q. Jia and S. Zhang were funded by the National Key Research and Development Program of China (Grant Number 2025YFE0102300. S. Chen received support from National Key Research and Development Program of China 2023YFF0806100 and NSFC Grant 42103081. JMW was supported by National Science Foundation Grant EAR1749183.

References

Abram, N. J., Gagan, M. K., Cole, J. E., Hantoro, W. S., & Mudelsee, M. (2008). Recent intensification of tropical climate variability in the Indian Ocean. *Nature Geoscience*, *1*(12), 849–853. https://doi.org/10.1038/ngeo357

Abram, N. J., Gagan, M. K., Liu, Z., Hantoro, W. S., McCulloch, M. T., & Suwargadi, B. W. (2007). Seasonal characteristics of the Indian ocean dipole during the holocene epoch. *Nature*, *445*(7125), 299–302. https://doi.org/10.1038/nature05477

Adkins, J. F., Boyle, E. A., Curry, W., & Lutringer, A. (2003). Stable isotopes in deep-sea corals and a new mechanism for "vital effects". *Geochimica et Cosmochimica Acta*, *67*(6), 1129–1143. https://doi.org/10.1016/s0016-7037(02)01203-6

Al-Horani, F., Al-Moghrabi, S., & De Beer, D. (2003a). The mechanism of calcification and its relation to photosynthesis and respiration in the scleractinian coral Galaxea fascicularis. *Marine Biology*, *142*(3), 419–426. https://doi.org/10.1007/s00227-002-0981-8

Al-Horani, F. A., Al-Moghrabi, S. M., & de Beer, D. (2003b). Microsensor study of photosynthesis and calcification in the scleractinian coral, Galaxea fascicularis: Active internal carbon cycle. *Journal of Experimental Marine Biology and Ecology*, *288*(1), 1–15. https://doi.org/10.1016/s0022-0981(02)00578-6

Allison, N., Venn, A., Tambutte, S., Tambutte, E., Wilckens, F., Kasemann, S., et al. (2023). A comparison of SNARF-1 and skeletal $\delta^{11}B$ estimates of calcification media pH in tropical coral. *Geochimica et Cosmochimica Acta*, *355*, 184–194. https://doi.org/10.1016/j.gca.2023.07.005

Bajnai, D., Guo, W., Spötl, C., Coplen, T. B., Methner, K., Löffler, N., et al. (2020). Dual clumped isotope thermometry resolves kinetic biases in carbonate formation temperatures. *Nature Communications*, *11*(1), 4005. https://doi.org/10.1038/s41467-020-17501-0

Bucher, D. J., Harriott, V. J., & Roberts, L. G. (1998). Skeletal micro-density, porosity and bulk density of acroporid corals. *Journal of Experimental Marine Biology and Ecology*, *228*(1), 117–136. https://doi.org/10.1016/s0022-0981(98)00020-3

Came, R. E., Brand, U., & Affek, H. P. (2014). Clumped isotope signatures in modern brachiopod carbonate. *Chemical Geology*, *377*, 20–30. https://doi.org/10.1016/j.chemgeo.2014.04.004

Canesi, M., Douville, É., Bordier, L., Dapoigny, A., Coulibaly, G. E., Montagna, P., et al. (2024). Porites' coral calcifying fluid chemistry regulation under normal-and low-pH seawater conditions in Palau Archipelago: Impacts on growth properties. *Science of the Total Environment*, *911*, 168552. https://doi.org/10.1016/j.scitotenv.2023.168552

Canesi, M., Douville, É., Montagna, P., Taviani, M., Stolarski, J., Bordier, L., et al. (2023). Differences in carbonate chemistry up-regulation of long-lived reef-building corals. *Scientific Reports*, *13*(1), 11589. https://doi.org/10.1038/s41598-023-37598-9

Chen, S., Gagnon, A. C., & Adkins, J. F. (2018). Carbonic anhydrase, coral calcification and a new model of stable isotope vital effects. *Geochimica et Cosmochimica Acta*, *236*, 179–197. https://doi.org/10.1016/j.gca.2018.02.032

Chen, S., & Watkins, J. M. (2025). Oxygen and carbon isotopes in marine carbonates: A biogenic climate archive built upon disequilibria. *Elements*, *21*(2), 112–117. https://doi.org/10.2138/gselements.21.2.112

Christensen, J. N., Watkins, J. M., Devriendt, L. S., DePaolo, D. J., Conrad, M. E., Voltolini, M., et al. (2021). Isotopic fractionation accompanying CO_2 hydroxylation and carbonate precipitation from high pH waters at the Cedars, California, USA. *Geochimica et Cosmochimica Acta*, *301*, 91–115. https://doi.org/10.1016/j.gca.2021.01.003

Clark, I. D., Fontes, J.-C., & Fritz, P. (1992). Stable isotope disequilibria in travertine from high pH waters: Laboratory investigations and field observations from Oman. *Geochimica et Cosmochimica Acta*, *56*(5), 2041–2050. https://doi.org/10.1016/0016-7037(92)90328-g

Cobb, K. M., Charles, C. D., Cheng, H., & Edwards, R. L. (2003). El Niño/Southern Oscillation and tropical Pacific climate during the last millennium. *Nature*, *424*(6946), 271–276. https://doi.org/10.1038/nature01779

Cobb, K. M., Westphal, N., Sayani, H. R., Watson, J. T., Di Lorenzo, E., Cheng, H., et al. (2013). Highly variable El Niño–southern oscillation throughout the holocene. *Science*, *339*(6115), 67–70. https://doi.org/10.1126/science.1228246

Cohen, A. L., & McConnaughey, T. A. (2003). Geochemical perspectives on coral mineralization. *Reviews in Mineralogy and Geochemistry*, *54*(1), 151–187. https://doi.org/10.2113/0540151

Cole, J. E., Fairbanks, R. G., & Shen, G. T. (1993). Recent variability in the southern oscillation: Isotopic results from a Tarawa atoll coral. *Science*, *260*(5115), 1790–1793. https://doi.org/10.1126/science.260.5115.1790

Comeau, S., Tambutté, E., Carpenter, R., Edmunds, P., Evensen, N., Allemand, D., et al. (2017). Coral calcifying fluid pH is modulated by seawater carbonate chemistry not solely seawater pH. *Proceedings of the Royal Society B: Biological Sciences*, *284*(1847), 20161669. https://doi.org/10.1098/rspb.2016.1669

Corrège, T., Gagan, M. K., Beck, J. W., Burr, G. S., Cabioch, G., & Le Cornec, F. (2004). Interdecadal variation in the extent of South Pacific tropical waters during the Younger Dryas event. *Nature*, *428*(6986), 927–929. https://doi.org/10.1038/nature02506

Cuif, J.-P., & Dauphin, Y. (2005). The two-step mode of growth in the scleractinian coral skeletons from the micrometre to the overall scale. *Journal of Structural Biology*, *150*(3), 319–331. https://doi.org/10.1016/j.jsb.2005.03.004

Davies, A., Brand, U., Tagliavento, M., Bitner, M., Bajnai, D., Staudigel, P., et al. (2023). Isotopic disequilibrium in brachiopods disentangled with dual clumped isotope thermometry. *Geochimica et Cosmochimica Acta*, *359*, 135–147. https://doi.org/10.1016/j.gca.2023.08.005

Davies, A., Guo, W., Bernecker, M., Tagliavento, M., Raddatz, J., Gischler, E., et al. (2022). Dual clumped isotope thermometry of coral carbonate. *Geochimica et Cosmochimica Acta*, *338*, 66–78. https://doi.org/10.1016/j.gca.2022.10.015

Defliese, W. F., & Lohmann, K. C. (2015). Non-linear mixing effects on mass-47 CO_2 clumped isotope thermometry: Patterns and implications. *Rapid Communications in Mass Spectrometry*, *29*(9), 901–909. https://doi.org/10.1002/rcm.7175

Devriendt, L. S., Watkins, J. M., & McGregor, H. V. (2017). Oxygen isotope fractionation in the $CaCO_3$-DIC-H_2O system. *Geochimica et Cosmochimica Acta*, *214*, 115–142. https://doi.org/10.1016/j.gca.2017.06.022

Dunbar, R. B., Wellington, G. M., Colgan, M. W., & Glynn, P. W. (1994). Eastern Pacific sea surface temperature since 1600 AD: The $\delta^{18}O$ record of climate variability in Galápagos corals. *Paleoceanography*, *9*(2), 291–315. https://doi.org/10.1029/93pa03501

Eagle, R., Eiler, J. M., Tripati, A., Ries, J., Freitas, P., Hiebenthal, C., et al. (2013). The influence of temperature and seawater carbonate saturation state on ^{13} c-^{18}O bond ordering in bivalve mollusks. *Biogeosciences*, *10*(7), 4591–4606. https://doi.org/10.5194/bg-10-4591-2013

Emiliani, C., Hudson, J. H., Shinn, E. A., & George, R. Y. (1978). Oxygen and carbon isotopic growth record in a reef coral from the Florida Keys and a deep-sea coral from Blake Plateau. *Science*, *202*(4368), 627–629. https://doi.org/10.1126/science.202.4368.627

Fairbanks, R. G., & Dodge, R. E. (1979). Annual periodicity of the $^{18}O/^{16}O$ and $^{13}C/^{12}C$ ratios in the coral *montastrea annularis*. *Geochimica et Cosmochimica Acta*, *43*(7), 1009–1020. https://doi.org/10.1016/0016-7037(79)90090-5

Fiebig, J., Daëron, M., Bernecker, M., Guo, W., Schneider, G., Boch, R., et al. (2021). Calibration of the dual clumped isotope thermometer for carbonates. *Geochimica et Cosmochimica Acta*, *312*, 235–256. https://doi.org/10.1016/j.gca.2021.07.012

Fietzke, J., & Wall, M. (2022). Distinct fine-scale variations in calcification control revealed by high-resolution 2D boron laser images in the cold-water coral *Lophelia pertusa*. *Science Advances*, *8*(11), eabj4172. https://doi.org/10.1126/sciadv.abj4172

Freund, M. B., Henley, B. J., Karoly, D. J., McGregor, H. V., Abram, N. J., & Dommenget, D. (2019). Higher frequency of Central Pacific El Niño events in recent decades relative to past centuries. *Nature Geoscience*, *12*(6), 450–455. https://doi.org/10.1038/s41561-019-0353-3

Gilbert, P. U., Bergmann, K. D., Boekelheide, N., Tambutté, S., Mass, T., Marin, F., et al. (2022). Biomineralization: Integrating mechanism and evolutionary history. *Science Advances*, *8*(10), eabl9653. https://doi.org/10.1126/sciadv.abl9653

Grauel, A.-L., Schmid, T. W., Hu, B., Bergami, C., Capotondi, L., Zhou, L., & Bernasconi, S. M. (2013). Calibration and application of the "clumped isotope" thermometer to foraminifera for high-resolution climate reconstructions. *Geochimica et Cosmochimica Acta*, *108*, 125–140. https://doi.org/10.1016/j.gca.2012.12.049

Guo, W. (2020). Kinetic clumped isotope fractionation in the DIC-H_2O-CO_2 system: Patterns, controls, and implications. *Geochimica et Cosmochimica Acta*, *268*, 230–257. https://doi.org/10.1016/j.gca.2019.07.055

Guo, W., & Zhou, C. (2019). Patterns and controls of disequilibrium isotope effects in speleothems: Insights from an isotope-enabled diffusion-reaction model and implications for quantitative thermometry. *Geochimica et Cosmochimica Acta*, *267*, 196–226. https://doi.org/10.1016/j.gca.2019.07.028

Henkes, G. A., Passey, B. H., Wanamaker Jr, A. D., Grossman, E. L., Ambrose Jr, W. G., & Carroll, M. L. (2013). Carbonate clumped isotope compositions of modern marine mollusk and brachiopod shells. *Geochimica et Cosmochimica Acta*, *106*, 307–325. https://doi.org/10.1016/j.gca.2012.12.020

Hill, P. S., Schauble, E. A., & Tripati, A. (2020). Theoretical constraints on the effects of added cations on clumped, oxygen, and carbon isotope signatures of dissolved inorganic carbon species and minerals. *Geochimica et Cosmochimica Acta*, *269*, 496–539. https://doi.org/10.1016/j.gca.2019.10.016

Hillaire-Marcel, C., Kim, S.-T., Landais, A., Ghosh, P., Assonov, S., Lécuyer, C., et al. (2021). A stable isotope toolbox for water and inorganic carbon cycle studies. *Nature Reviews Earth and Environment*, *2*(10), 699–719. https://doi.org/10.1038/s43017-021-00209-0

Holcomb, M., Venn, A., Tambutté, E., Tambutté, S., Allemand, D., Trotter, J., & Mcculloch, M. (2014). Coral calcifying fluid pH dictates response to ocean acidification. *Scientific Reports*, *4*(1), 5207. https://doi.org/10.1038/srep05207

Hopkinson, B. M., Tansik, A. L., & Fitt, W. K. (2015). Internal carbonic anhydrase activity in the tissue of scleractinian corals is sufficient to support proposed roles in photosynthesis and calcification. *Journal of Experimental Biology*, *218*(13), 2039–2048.

Ip, Y., & Krishnaveni, P. (1991). Incorporation of strontium ($^{90}Sr^{2+}$) into the skeleton of the hermatypic coral Galaxea fascicularis. *Journal of Experimental Zoology*, *258*(2), 273–276. https://doi.org/10.1002/jez.1402580219

Jiang, L. Q., Carter, B. R., Feely, R. A., Lauvset, S. K., & Olsen, A. (2019). Surface ocean pH and buffer capacity: past, present and future. *Scientific Reports*, *9*, 18624. https://doi.org/10.1038/s41598-019-55039-4

Katz, A., Bonifacie, M., Hermoso, M., Cartigny, P., & Calmels, D. (2017). Laboratory-grown coccoliths exhibit no vital effect in clumped isotope (δ47) composition on a range of geologically relevant temperatures. *Geochimica et Cosmochimica Acta*, *208*, 335–353. https://doi.org/10.1016/j.gca.2017.02.025

Kingsley, R. J., & Watabe, N. (1984). Calcium uptake in the gorgonian Leptogorgia virgulata. the effects of ATPase inhibitors. *Comparative Biochemistry and Physiology Part A: Physiology*, *79*(3), 487–491. https://doi.org/10.1016/0300-9629(84)90551-6

Kingsley, R. J., & Watabe, N. (1987). Role of carbonic anhydrase in calcification in the gorgonian Leptogorgia virgulata. *Journal of Experimental Zoology*, *241*(2), 171–180. https://doi.org/10.1002/jez.1402410203

Kinsman, D. J. (1969). Interpretation of $Sr^{2=}$concentrations in carbonate minerals and rocks. *Journal of Sedimentary Research*, *39*(2), 486–508.

Krief, S., Hendy, E. J., Fine, M., Yam, R., Meibom, A., Foster, G. L., & Shemesh, A. (2010). Physiological and isotopic responses of scleractinian corals to ocean acidification. *Geochimica et Cosmochimica Acta*, *74*(17), 4988–5001. https://doi.org/10.1016/j.gca.2010.05.023

Mass, T., Drake, J. L., Peters, E. C., Jiang, W., & Falkowski, P. G. (2014). Immunolocalization of skeletal matrix proteins in tissue and mineral of the coral *Stylophora pistillata*. *Proceedings of the National Academy of Sciences*, *111*(35), 12728–12733. https://doi.org/10.1073/pnas.1408621111

Mass, T., Giuffre, A. J., Sun, C.-Y., Stifler, C. A., Frazier, M. J., Neder, M., et al. (2017). Amorphous calcium carbonate particles form coral skeletons. *Proceedings of the National Academy of Sciences*, *114*(37), E7670–E7678. https://doi.org/10.1073/pnas.1707890114

McConnaughey, T. (1989a). ^{13}C and ^{18}O isotopic disequilibrium in biological carbonates: I. Patterns. *Geochimica et Cosmochimica Acta*, *53*(1), 151–162. https://doi.org/10.1016/0016-7037(89)90282-2

McConnaughey, T. (1989b). ^{13}C and ^{18}O isotopic disequilibrium in biological carbonates: II. In vitro simulation of kinetic isotope effects. *Geochimica et Cosmochimica Acta*, *53*(1), 163–171. https://doi.org/10.1016/0016-7037(89)90283-4

McCulloch, M., Falter, J., Trotter, J., & Montagna, P. (2012). Coral resilience to ocean acidification and global warming through pH up-regulation. *Nature Climate Change*, *2*(8), 623–627. https://doi.org/10.1038/nclimate1473

McCulloch, M. T., D'Olivo, J. P., Falter, J., Holcomb, M., & Trotter, J. A. (2017). Coral calcification in a changing world and the interactive dynamics of pH and DIC upregulation. *Nature Communications*, *8*(1), 15686. https://doi.org/10.1038/ncomms15686

McGregor, H. V., & Gagan, M. K. (2004). Western Pacific coral $\delta^{18}O$ records of anomalous holocene variability in the El Niño–southern oscillation. *Geophysical Research Letters*, *31*(11), L11204. https://doi.org/10.1029/2004gl019972

Meinicke, N., Ho, S., Hannisdal, B., Nürnberg, D., Tripati, A., Schiebel, R., & Meckler, A. (2020). A robust calibration of the clumped isotopes to temperature relationship for foraminifers. *Geochimica et Cosmochimica Acta*, *270*, 160–183. https://doi.org/10.1016/j.gca.2019.11.022

Moya, A., Tambutté, S., Bertucci, A., Tambutté, E., Lotto, S., Vullo, D., et al. (2008). Carbonic anhydrase in the scleractinian coral *Stylophora pistillata*: Characterization, localization, and role in biomineralization. *Journal of Biological Chemistry*, *283*(37), 25475–25484.

Peral, M., Daëron, M., Blamart, D., Bassinot, F., Dewilde, F., Smialkowski, N., et al. (2018). Updated calibration of the clumped isotope thermometer in planktonic and benthic foraminifera. *Geochimica et Cosmochimica Acta*, *239*, 1–16. https://doi.org/10.1016/j.gca.2018.07.016

Piasecki, A., Bernasconi, S. M., Grauel, A.-L., Hannisdal, B., Ho, S. L., Leutert, T. J., et al. (2019). Application of clumped isotope thermometry to benthic foraminifera. *Geochemistry, Geophysics, Geosystems*, *20*(4), 2082–2090. https://doi.org/10.1029/2018gc007961

Robinson, L. F., Adkins, J. F., Frank, N., Gagnon, A. C., Prouty, N. G., Roark, E. B., & Van de Flierdt, T. (2014). The geochemistry of deep-sea coral skeletons: A review of vital effects and applications for palaeoceanography. *Deep Sea Research Part II: Topical Studies in Oceanography*, *99*, 184–198.

Rollion-Bard, C., Chaussidon, M., & France-Lanord, C. (2011). Biological control of internal pH in scleractinian corals: Implications on paleo-pH and paleo-temperature reconstructions. *Comptes Rendus Geoscience*, *343*(6), 397–405. https://doi.org/10.1016/j.crte.2011.05.003

Romanek, C. S., Grossman, E. L., & Morse, J. W. (1992). Carbon isotopic fractionation in synthetic aragonite and calcite: Effects of temperature and precipitation rate. *Geochimica et Cosmochimica Acta*, *56*(1), 419–430. https://doi.org/10.1016/0016-7037(92)90142-6

Ross, C. L., Warnes, A., Comeau, S., Cornwall, C. E., Cuttler, M. V., Naugle, M., et al. (2022). Coral calcification mechanisms in a warming ocean and the interactive effects of temperature and light. *Communications Earth and Environment*, *3*(1), 72. https://doi.org/10.1038/s43247-022-00396-8

Saenger, C., Affek, H. P., Felis, T., Thiagarajan, N., Lough, J. M., & Holcomb, M. (2012). Carbonate clumped isotope variability in shallow water corals: Temperature dependence and growth-related vital effects. *Geochimica et Cosmochimica Acta*, *99*, 224–242. https://doi.org/10.1016/j.gca.2012.09.035

Saenger, C., & Erez, J. (2016). A non-traditional stable isotope perspective on coral calcification. *The Cnidaria, Past, Present and Future: The world of Medusa and her sisters*, 181–205.

Schmidt, C. A., Tambutté, E., Venn, A. A., Zou, Z., Castillo Alvarez, C., Devriendt, L. S., et al. (2024). Myriad mapping of nanoscale minerals reveals calcium carbonate hemihydrate in forming nacre and coral biominerals. *Nature Communications*, *15*(1), 1812. https://doi.org/10.1038/s41467-024-46117-x

Sevilgen, D. S., Venn, A. A., Hu, M. Y., Tambutté, E., de Beer, D., Planas-Bielsa, V., & Tambutté, S. (2019). Full in vivo characterization of carbonate chemistry at the site of calcification in corals. *Science Advances*, *5*(1), eaau7447. https://doi.org/10.1126/sciadv.aau7447

Spooner, P. T., Guo, W., Robinson, L. F., Thiagarajan, N., Hendry, K. R., Rosenheim, B. E., & Leng, M. J. (2016). Clumped isotope composition of cold-water corals: A role for vital effects? *Geochimica et Cosmochimica Acta*, *179*, 123–141. https://doi.org/10.1016/j.gca.2016.01.023

Sültemeyer, D., & Rinast, K.-A. (1996). The CO_2 permeability of the plasma membrane of Chlamydomonas reinhardtii: Mass-spectrometric ^{18}O-exchange measurements from $^{13}C^{18}O_2$ in suspensions of carbonic anhydrase-loaded plasma-membrane vesicles. *Planta*, *200*(3), 358–368. https://doi.org/10.1007/bf00200304

Sun, C.-Y., Stifler, C. A., Chopdekar, R. V., Schmidt, C. A., Parida, G., Schoeppler, V., et al. (2020). From particle attachment to space-filling coral skeletons. *Proceedings of the National Academy of Sciences*, *117*(48), 30159–30170. https://doi.org/10.1073/pnas.2012025117

Swart, P. K. (1983). Carbon and oxygen isotope fractionation in scleractinian corals: A review. *Earth-Science Reviews*, *19*(1), 51–80. https://doi.org/10.1016/0012-8252(83)90076-4

Tambutté, S., Tambutté, E., Zoccola, D., Caminiti, N., Lotto, S., Moya, A., et al. (2007). Characterization and role of carbonic anhydrase in the calcification process of the azooxanthellate coral tubastrea aurea. *Marine Biology*, *151*(1), 71–83. https://doi.org/10.1007/s00227-006-0452-8

Tierney, J. E., Abram, N. J., Anchukaitis, K. J., Evans, M. N., Giry, C., Kilbourne, K. H., et al. (2015). Tropical sea surface temperatures for the past four centuries reconstructed from coral archives. *Paleoceanography*, *30*(3), 226–252. https://doi.org/10.1002/2014pa002717

Tinoco, A. I., Mitchison-Field, L. M., Bradford, J., Renicke, C., Perrin, D., Bay, L. K., et al. (2023). Role of the bicarbonate transporter SLC4γ in stony-coral skeleton formation and evolution. *Proceedings of the National Academy of Sciences*, *120*(24), e2216144120. https://doi.org/10.1073/pnas.2216144120

Tripati, A. K., Eagle, R. A., Thiagarajan, N., Gagnon, A. C., Bauch, H., Halloran, P. R., & Eiler, J. M. (2010). ^{13}C-^{18}O isotope signatures and "clumped isotope" thermometry in foraminifera and coccoliths. *Geochimica et Cosmochimica Acta*, *74*(20), 5697–5717. https://doi.org/10.1016/j.gca.2010.07.006

Trotter, J., Montagna, P., McCulloch, M., Silenzi, S., Reynaud, S., Mortimer, G., et al. (2011). Quantifying the pH "vital effect" in the temperate zooxanthellate coral *Cladocora caespitosa*: Validation of the boron seawater pH proxy. *Earth and Planetary Science Letters*, *303*(3–4), 163–173. https://doi.org/10.1016/j.epsl.2011.01.030

Tudhope, A. W., Chilcott, C. P., McCulloch, M. T., Cook, E. R., Chappell, J., Ellam, R. M., et al. (2001). Variability in the El Niño-southern oscillation through a glacial-interglacial cycle. *Science*, *291*(5508), 1511–1517. https://doi.org/10.1126/science.1057969

Uchikawa, J., Chen, S., Eiler, J. M., Adkins, J. F., & Zeebe, R. E. (2021). Trajectory and timescale of oxygen and clumped isotope equilibration in the dissolved carbonate system under normal and enzymatically-catalyzed conditions at 25°C. *Geochimica et Cosmochimica Acta*, *314*, 313–333. https://doi.org/10.1016/j.gca.2021.08.014

Venn, A., Tambutté, E., Caminiti-Segonds, N., Techer, N., Allemand, D., & Tambutté, S. (2019). Effects of light and darkness on pH regulation in three coral species exposed to seawater acidification. *Scientific Reports*, *9*(1), 2201. https://doi.org/10.1038/s41598-018-38168-0

Venn, A., Tambutté, E., Holcomb, M., Allemand, D., & Tambutté, S. (2011). Live tissue imaging shows reef corals elevate pH under their calcifying tissue relative to seawater. *PLoS One*, *6*(5), e20013. https://doi.org/10.1371/journal.pone.0020013

Venn, A. A., Tambutte, E., Comeau, S., & Tambutte, S. (2022). Proton gradients across the coral calcifying cell layer: Effects of light, ocean acidification and carbonate chemistry. *Frontiers in Marine Science*, *9*, 973908. https://doi.org/10.3389/fmars.2022.973908

Venn, A. A., Tambutté, E., Holcomb, M., Laurent, J., Allemand, D., & Tambutté, S. (2013). Impact of seawater acidification on pH at the tissue–skeleton interface and calcification in reef corals. *Proceedings of the National Academy of Sciences*, *110*(5), 1634–1639. https://doi.org/10.1073/pnas.1216153110

Vidal-Dupiol, J., Zoccola, D., Tambutté, E., Grunau, C., Cosseau, C., Smith, K. M., et al. (2013). Genes related to ion-transport and energy production are upregulated in response to CO_2-driven pH decrease in corals: New insights from transcriptome analysis. *PLoS One*, *8*(3), e58652. https://doi.org/10.1371/journal.pone.0058652

Wang, Z., Gaetani, G., Liu, C., & Cohen, A. (2013). Oxygen isotope fractionation between aragonite and seawater: Developing a novel kinetic oxygen isotope fractionation model. *Geochimica et Cosmochimica Acta*, *117*, 232–251. https://doi.org/10.1016/j.gca.2013.04.025

Watkins, J. (2025). COAD box model for corals. URL https://zenodo.org/records/15642426

Watkins, J., & Hunt, J. (2015). A process-based model for non-equilibrium clumped isotope effects in carbonates. *Earth and Planetary Science Letters*, *432*, 152–165. https://doi.org/10.1016/j.epsl.2015.09.042

Watkins, J. M., & Devriendt, L. S. (2022). A combined model for kinetic clumped isotope effects in the $CaCO_3$-DIC-H_2O system. *Geochemistry, Geophysics, Geosystems*, *23*(8), e2021GC010200. https://doi.org/10.1029/2021gc010200

Watkins, J. M., Hunt, J. D., Ryerson, F. J., & DePaolo, D. J. (2014). The influence of temperature, pH, and growth rate on the δ^{18}o composition of inorganically precipitated calcite. *Earth and Planetary Science Letters*, *404*, 332–343. https://doi.org/10.1016/j.epsl.2014.07.036

Watkins, J. M., Nielsen, L. C., Ryerson, F. J., & DePaolo, D. J. (2013). The influence of kinetics on the oxygen isotope composition of calcium carbonate. *Earth and Planetary Science Letters*, *375*, 349–360. https://doi.org/10.1016/j.epsl.2013.05.054

Weber, J. N., & Woodhead, P. M. (1970). Carbon and oxygen isotope fractionation in the skeletal carbonate of reef-building corals. *Chemical Geology*, *6*, 93–117. https://doi.org/10.1016/0009-2541(70)90009-4

Weber, J. N., & Woodhead, P. M. (1972). Temperature dependence of oxygen-18 concentration in reef coral carbonates. *Journal of Geophysical Research*, *77*(3), 463–473. https://doi.org/10.1029/jc077i003p00463

Wells, J. W. (1963). Coral growth and geochronometry. *Nature*, *197*(4871), 948–950. https://doi.org/10.1038/197948a0

Wolthers, M., Di Tommaso, D., Du, Z., & de Leeuw, N. H. (2012). Calcite surface structure and reactivity: Molecular dynamics simulations and macroscopic surface modelling of the calcite–water interface. *Physical Chemistry Chemical Physics*, *14*(43), 15145–15157. https://doi.org/10.1039/c2cp42290e

Yu, X., & Inesi, G. (1995). Variable stoichiometric efficiency of Ca^{2+} and Sr^{2+} transport by the sarcoplasmic reticulum ATPase. *Journal of Biological Chemistry*, *270*(9), 4361–4367. https://doi.org/10.1074/jbc.270.9.4361

Yumol, L. M., Uchikawa, J., & Zeebe, R. E. (2020). Kinetic isotope effects during CO_2 hydration: Experimental results for carbon and oxygen fractionation. *Geochimica et Cosmochimica Acta*, *279*, 189–203. https://doi.org/10.1016/j.gca.2020.03.041

Zeebe, R. E. (2020). Oxygen isotope fractionation between water and the aqueous hydroxide ion. *Geochimica et Cosmochimica Acta*, *289*, 182–195.

Zeebe, R. E., & Wolf-Gladrow, D. (2001). *CO_2 in seawater: equilibrium, kinetics, isotopes. No. 65*. Gulf Professional Publishing.

Zoccola, D., Ganot, P., Bertucci, A., Caminiti-Segonds, N., Techer, N., Voolstra, C. R., et al. (2015). Bicarbonate transporters in corals point towards a key step in the evolution of cnidarian calcification. *Scientific Reports*, *5*(1), 9983. https://doi.org/10.1038/srep09983